Electronic Supplementary Material (ESI) for Journal of Materials Chemistry A.

Supplementary Information

Conor Jason Price,* Edward Allery David Baker, and Steven Paul Hepplestone†

Department of Physics, University of Exeter,

Stocker Road, Exeter, EX4 4QL, United Kingdom

CONTENTS

I. METHODOLOGY

A. Calculation Details

In Table SI, the valence electrons considered for each species are presented. All other electrons were effectively contained within the used pseudopotentials. The projector augmented wave method[1] was used to describe the interaction between core and valence electrons, and a plane-wave basis set was used with an energy cutoff of 700 eV. Monkhorst-Pack grids[2] of k-points equivalent to a $6 \times 6 \times 6$ grid in the supercells (discussed later) are used throughout. The Perdew-Burke-Ernzerhof (PBE)[3] functional form of the generalised gradient approximation (GGA) was used with the van der Waals interactions addressed using the zero damping DFT-D3 method of Grimme[4]. The PBE functional has been widely observed to inaccurately consider exchange effects, which can lead to significant changes in results. We have therefore also performed a limited study using the HSE06 functional, the results of which are presented below. All structural relaxations were completed using the PBE functional[3] using the conjugate gradient algorithm and converged to a force tolerance of 0.01 eV/Å per atom, and electronic self-consistency is considered to an accuracy of 10^{-7} eV.

Electronic band structures were obtained along the route Γ-M-K-Γ-A-L-H-A, where we track the shift in the position of the highest occupied molecular orbital (HOMO) with intercalation by alignment of the band structures of the pristine, lithium-intercalated, and magnesium-intercalated structures. Alignment of electronic band structures is usually achieved either through alignment of core states[5] or through alignment with respect to the vacuum level[5–7]. However, charge transfer upon intercalation (as shall be discussed later) leads to local electric dipoles that shift the position of even deep core states, and so core alignment is not appropriate. Alignment with respect to the vacuum level, on the other hand, requires the inclusion of a vacuum region within the system. To maintain stoichiometry, one surface would need to consist of intercalant ions and the opposite layer should be a bare TMDC layer, which naturally leads to large electric fields across the vacuum region. To avoid these large electric fields, both surfaces should be symmetrically equivalent, but this then breaks the stoichiometry of the compound in question. As such, we have instead chosen to qualitatively align the high-energy occupied states of the pristine and intercalated structures at Γ, allowing us to comment on the position of the HOMO level.

Species	Included Electrons	Species	Included Electrons
Li	$1s^2 2s^1$ (3)	Re	$5d^6 6s^1$ (7)
Mg	$2p^6 3s^2$ (8)	Fe	$3d^7 4s^1$ (8)
S	$3s^2 3p^4$ (6)	Ru	$4s^2 4p^6 4d^7 5s^1$ (16)
Se	$4s^2 4p^4$ (6)	Os	$5d^7 6s^1$ (8)
Te	$5s^2 5p^4$ (6)	Co	$3d^8 4s^1$ (9)
Sc	$3d^2 4s^1$ (3)	Rh	$4d^8 5s^1$ (9)
Y	$4s^2 4p^6 4d^2$ (10)	Ir	$5d^8 6s^1$ (9)
Ti	$3p^6 3d^3 4s^1$ (10)	Ni	$3d^9 4s^1$ (10)
Zr	$4s^2 4p^6 4d^3$ (11)	Pd	$4d^9 5s^1$ (10)
Hf	$5d^3 6s^1$ (4)	Pt	$5d^9 6s^1$ (10)
V	$3d^4 4s^1$ (5)	Cu	$3d^{10} 4s^1$ (11)
Nb	$4s^2 4p^6 4d^4 5s^1$ (13)	Ag	$4d^{10} 5s^1$ (11)
Ta	$5d^4 6s^1$ (5)	Au	$5d^{10} 6s^1$ (11)
Cr	$3s^2 4s^1 4p^6 4d^5$ (14)	Ge	$3d^{10} 4s^2 4p^2$ (14)
Mo	$4d^5 5s^1$ (6)	Sn	$4d^{10} 5s^2 5p^2$ (14)
W	$5d^5 6s^1$ (6)	Pb	$5d^{10} 6s^2 6p^2$ (14)
Mn	$3p^6 3d^6 4s^1$ (13)		

Table S I: Electronic configurations of electrons modelled for different species considered in this study.

B. Intercalation Configuration

A $2 \times 2 \times 2$ supercell of the TMDC structures were used for the following investigation. For the supercell size used, there were eight symmetrically equivalent octahderal sites for intercalation, shown in Figure S1. This results in 23 potential interalated configurations (listed in Table SII) which were each explored. First, each of the 23 configurations were generated, independently of each other, and geometric relaxations performed. This sometimes led to discontinuities in the voltage profiles and the geometric structures. To address this, a second method used was to take geometrically relaxed structures with lower intercalant concentrations, introduce more of the intercalant, and continue the geometric relaxation from there. For a given concentration, the structure with the lowest energy from either of the two methods was used.

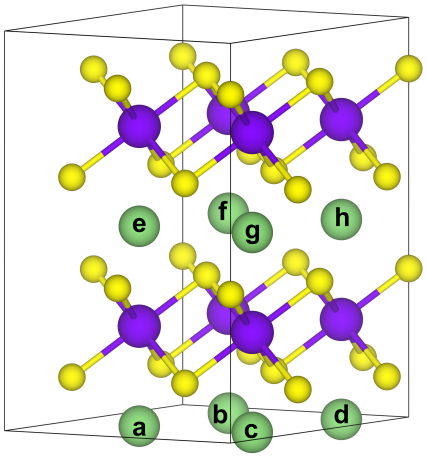

Figure S 1: The different intercalation sites available in the supercells of T-phase TMDCs considered in this work, indexed a-h.

No. Li Atoms	Sites Filled	No. Li Atoms	Sites Filled
0	-	4	adeh
1	a	4	adfg
2	ab	4	adfh
2	ae	5	abcde
2	af	5	abcef
2	ah	5	abceh
3	abc	6	abcdef
3	abe	6	abcefg
3	bce	6	abdefg
4	abcd	6	bcdefg
4	abce	7	abcdefg
4	abch	8	abcdefgh

Table S II: Table showing the 24 different intercalation configurations (including the unintercalated) considered for the intercalation of MX_2 materials for nine different lithium concentrations.

C. Calculation of Voltage

To compare different levels of intercalated MX_2-materials the voltage, V, can be calculated using[8,9],

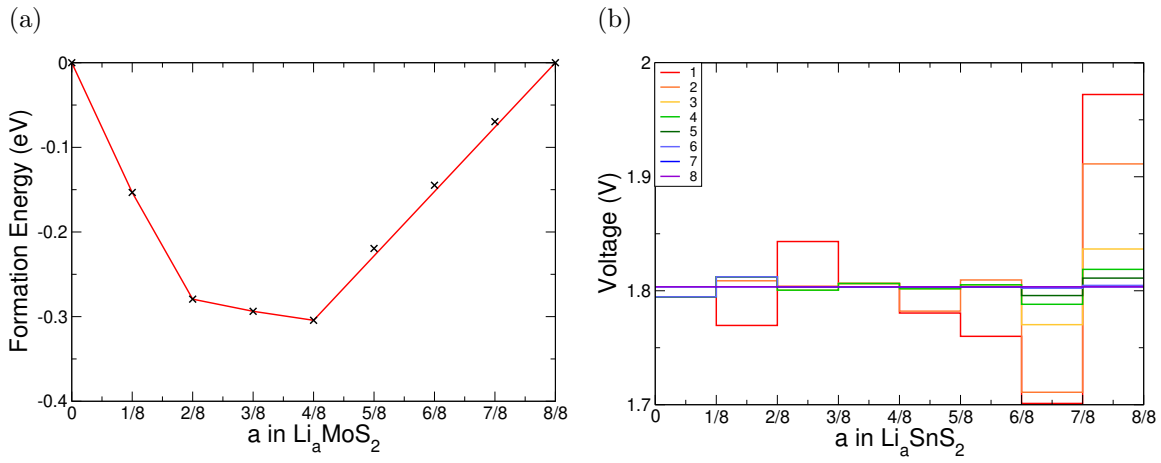

Figure S 2: The convex hull for Li_aMoS_2 is shown in S2a, and the effect on the resultant voltage (for Li_aSnS_2) from changing the number of components involved in calculating the lowest energy for a given lithium concentration is given in S2b.

$$\begin{aligned} V &= -\frac{\Delta G}{\Delta Q} \\ &\approx -\frac{\Delta E}{\Delta Q} \\ &= -\frac{E_{\mathrm{Li}_{a_2}\mathrm{MX}} - \left[E_{\mathrm{Li}_{a_1}\mathrm{MX}_2} + (a_2 - a_1)E_{\mathrm{Li}}\right]}{(a_2 - a_1)e} \end{aligned} \tag{S1}$$

for change in Gibbs free energy, ΔG, total lithium content $a_1 < a_2$, $E_{\mathrm{Li}_a\mathrm{MX}_2}$ is the energy of the supercell bulk MX_2 structure with a lithium atoms per MX_2 formula unit, and E_{Li} is the energy of a lithium atom as found in bulk[10]. This provides a voltage vs. Li/Li^+, and all voltages presented in this work will be given using this reference. Analogous equations were used for superlattice voltage calculations. Above, the Gibbs free energy is approximated as the internal energy, as the pressure-volume and vibrational entropy contributions are negligible[8].

Whilst we have evaluated the total energy for different levels of intercalation, the true lowest energy for a specific intercalant concentration might not be achievable for the unit cell size being modelled with DFT methods. Instead, a combination of different concentrations (the total concentration equalling the target concentration) might instead be preferred. For example, whilst we have evaluated the energy for a supercell containing four lithium atoms, a lower energy might instead be obtained by the average of a totally empty cell and a fully

intercalated cell, i.e. $E_4 > \frac{1}{8}(4E_0 + 4E_8)$. In cases like this, the intercalated structure would have a phase separation, with fully intercalated regions and completely empty regions instead of a homogeneous lithium distribution. This simple example can be extended to include other components and different numbers of components, which can have dramatic effects on the resulting voltage profiles.

This is easily visualised by consideration of the convex hull: Figure S2a presents the convex hull for Li_aMoS_2 using the formation energy calculated using

$$V = E_{\mathrm{Li}_a\mathrm{MoS}_2} - \Big[aE_{\mathrm{LiMoS}_2} + (1-a)E_{\mathrm{MoS}_2}\Big]. \tag{S2}$$

Whilst the energies $E_{Li_aMoS_2}$ lie on the hull for $0 \leq a \leq \frac{4}{8}$, concentrations of $a = \frac{5}{8}, \frac{6}{8}, \frac{7}{8}$ lie above it, and so a combination of the energies $E_{Li_{\frac{4}{8}}MoS_2}$ and E_{LiMoS_2} are required.

This is also shown for SnS_2 in Figure S2, where the effect of the number of components included is highlighted. The point at which the voltage profile becomes constant or decreasing with lithium concentration gives the correct profile. As shown in Figure S2, and in the figures of the main article, the voltage for SnS_2 is constant across the intercalation range. This is due to the fact that, for each of the concentrations, it is energetically preferred for the lithium to separate into regions with no lithium (with an energy of E_0) and regions that are fully intercalated (with and energy of E_8). For example, the lowest energy for $\mathrm{Li}_{\frac{1}{8}}\mathrm{SnS}_2$ is given by $E_1 = \frac{1}{8}(7E_0+E_8)$, and the lowest energy for $\mathrm{Li}_{\frac{2}{8}}\mathrm{SnS}_2$ is given by $E_2 = \frac{1}{8}(6E_0+2E_8)$. As the difference between consecutive concentrations is a constant $\Delta E = \frac{1}{8}(E_8 - E_0)$, the voltage is also constant across the range.

D. Phase Diagram Derivation

For an arbitrary TMDC material, MX_2, when intercalated with lithium, $\mathrm{Li_aMX_2}$, we define the enthalpy of formation of relevant products:

$$\Delta H(\mathrm{Li_aMX_2}) = E(\mathrm{Li_aMX_2}) - [a\mu^0_{Li} + \mu^0_M + 2\mu^0_{\mathrm{X}}] \tag{S3}$$

$$\Delta H(\mathrm{MX_2}) = E(\mathrm{MX_2}) - [\mu^0_M + 2\mu^0_{\mathrm{X}}] \tag{S4}$$

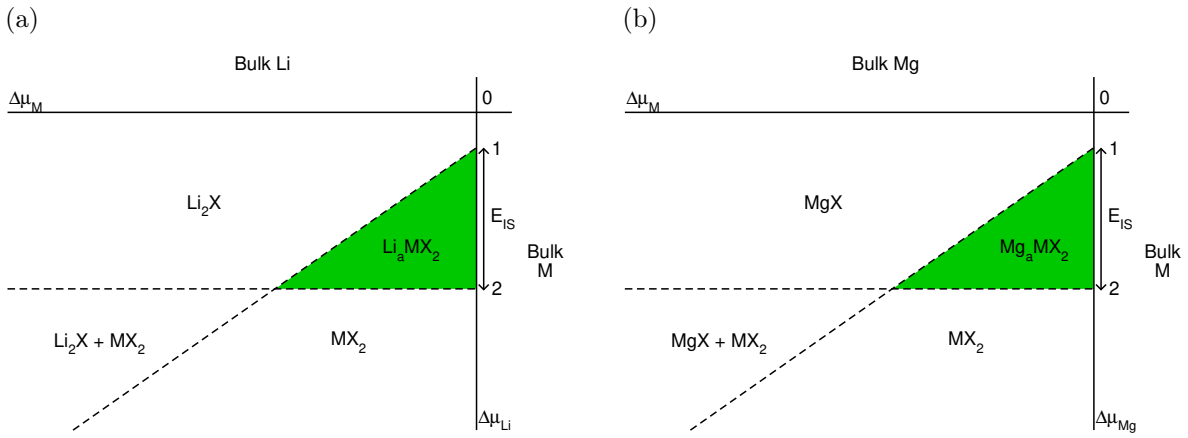

Figure S 3: Schematic phase diagrams for lithium (S3a) and magnesium (S3b) intercalated TMDCs, constructed using equations (S11)-(S12) and (S15).

$$\Delta H(\mathrm{Li_2X}) = E(\mathrm{Li_2X}) - [2\mu^0_{Li} + \mu^0_{\mathrm{X}}] \tag{S5}$$

where $\Delta H(A)$ gives the enthalpy of formation of the compound A, $E(A)$ gives the energy of the compound A, and $\mu^0_B = E(B)$ gives the chemical potential of elemental species B when it is in its elemental bulk structure.

The thermodynamic equilibrium condition requires,

$$\Delta H(\mathrm{Li_aMX_2}) = a\Delta\mu_{Li} + \Delta\mu_M + 2\Delta\mu_{\mathrm{X}}, \tag{S6}$$

where we have used the notation $\Delta\mu_B = \mu_B - \mu^0_B$, with μ_B being the chemical potential of elemental species B in $\mathrm{Li_aMX_2}$. This simply states that the energy of the superlattice structure is the sum of the chemical potentials of the constituent atoms. Rearranging the thermodynamic equilibrium condition gives,

$$\Delta\mu_{\mathrm{X}} = \frac{1}{2}\big\{\Delta H(\mathrm{Li_aMX_2}) - [a\Delta\mu_{Li} + \Delta\mu_M]\big\}. \tag{S7}$$

We require that $\mathrm{Li_2X}$, $\mathrm{MX_2}$, and the bulk forms of the component elements do not form. Therefore,

$$\Delta\mu_M + 2\Delta\mu_{\mathrm{X}} \leq \Delta H(\mathrm{MX_2}), \tag{S8}$$

$$2\Delta\mu_{Li} + \Delta\mu_{\mathrm{X}} \leq \Delta H(\mathrm{Li_2X}), \tag{S9}$$

$$\Delta\mu_{Li,M,X} \leq 0. \tag{S10}$$

Substituting (S7) into (S8) and rearranging,

$$\frac{1}{a}\big\{\Delta H(\mathrm{Li_aMX_2}) - \Delta H(\mathrm{MX_2})\big\} \leq \Delta\mu_{Li}. \tag{S11}$$

This then gives the thermodynamic limit on the lithium chemical potential such that the intercalation of the TMDC is preferred to the pristine TMDC and bulk lithium.

We now substitute (S7) into (S9) which results in,

$$\Delta\mu_{Li} \leq \frac{1}{4-a}\big[2\Delta H(\mathrm{Li_2X}) - \Delta H(\mathrm{Li_aMX_2}) + \Delta\mu_M\big], \tag{S12}$$

which is then the thermodynamic limit on the chemical potential of the lithium so that the conversion-reaction product $\mathrm{Li_2X}$ do not form.

Thus, we have two equations describing the boundary conditions for the chemical potential of lithium, dependent on formation energies of the relevant products, and the chemical potentials of the relevant metals, which are the equations presented in the main article.

We can equally consider the magnesium-compounds, and the limits on the chemical potential of magnesium. We start by defining the enthalpy of formation of MgX,

$$\Delta H(\mathrm{MgX}) = E(\mathrm{MgX}) - [\mu^0_{\mathrm{Mg}} + \mu^0_{\mathrm{X}}] \tag{S13}$$

Analogous to the condition (S9),

$$\Delta\mu_{\mathrm{Mg}} + \Delta\mu_{\mathrm{X}} \leq \Delta H(\mathrm{MgX}), \tag{S14}$$

which can be combined with the magnesium equivalent of (S7), to get,

$$\Delta\mu_{\mathrm{Mg}} \leq \frac{1}{2-a}\big[2\Delta H(\mathrm{MgX}) - \Delta H(\mathrm{Mg_aMX_2}) + \Delta\mu_M\big]. \tag{S15}$$

It should be noted, by considering the equations (S3)-(S5) and (S13), that the limiting conditions are independent of μ^0_{X},and hence $\Delta\mu_{\mathrm{X}}$. As a result, the phase diagrams are only dependent on the chemical potentials of lithium and the relevant metal, $\Delta\mu_{Li,Mg,M}$.

Using equations (S10)-(S12) and (S15), we can construct thermodynamic phase diagrams with the purpose of estimating the intercalation capacity.. Schematics of such phase diagrams are shown in Figure S3. We restrict ourselves to the negative-negative quadrant to ensure that the elemental bulks do not form. Above the diagonal line, labelled "1", the experimentally observed Li_2S (or equivalent) crystal is favoured, as opposed to the intercalated MX_2. Below the horizontal line, labelled "2", the pristine MX_2 structure is preferred to intercalation. The result of this is that intercalation is favoured for chemical potential combinations that sit within the shaded region indicated in Figure 1a of the main article. Outside of this window, however, the secondary products (as indicated in the figure) are favourable to form. Though a transition to these is not guaranteed, the intercalated MX_2 structure becomes meta-stable. Whilst other compounds could have their respective boundaries determined to be included in these phase diagrams, such as Li_2X_2 or MX, these first require the disintegration of the Li_aMX_2 material into Li_2X and/or elemental bulks. Hence, we only consider the limits outlined above.

To quantitatively compare the phase diagrams for the different concentrations considered, we can evaluate the difference between the intercepts of lines 1 and 2 with the $\Delta\mu_{Li}$-axis. E_{IS} is then defined as,

$$E_{IS} = \Delta\mu^{(1)}_{Li}(\Delta\mu_M = 0) - \Delta\mu^{(2)}_{Li}(\Delta\mu_M = 0), \tag{S16}$$

where $\Delta\mu^{(1/2)}_{Li}(\Delta\mu_M = 0)$ is the value of the boundary line 1/2 at the point where $\Delta\mu_M = 0$. Alternatively, using (S11) and (S12), E_{IS} can be expressed as,

$$E_{IS} = \frac{2}{4-a}\Delta H(\mathrm{Li_2X}) + \frac{1}{a}\Delta H(\mathrm{MX_2}) - \frac{4}{4a-a^2}\Delta H(\mathrm{Li_aMX_2}), \tag{S17}$$

in terms of the relevant formation enthalpy values. Each of the enthalpy of formation values should be negative for them to be thermodynamically stable with respect to their atomic constituents. When the value of E_{IS} is negative, the first two terms dominate, and line "1" intercepts below line "2" so no stability region exists. When the value of E_{IS} is positive, however, $\Delta H(\mathrm{Li_aSnS_2})$ dominates and the intercalated MX_2 material is stable. For magnesium intercalation, we have an equivalent expression using,

$$E_{IS} = \Delta\mu^{(1)}_{\mathrm{Mg}}(\Delta\mu_M = 0) - \Delta\mu^{(2)}_{\mathrm{Mg}}(\Delta\mu_M = 0), \tag{S18}$$

resulting in,

$$E^{Mg}_{IS} = \frac{2}{2-a}\Delta H(\mathrm{MgX}) + \frac{1}{a}\Delta H(\mathrm{MX_2}) - \frac{2}{2a-a^2}\Delta H(\mathrm{Mg_aMX_2}). \tag{S19}$$

E. Determination of Structure

Some materials are obviously susceptible to more significant structural changes, and do not exhibit a layered structure. $LiAuS_2$, $LiPtS_2$, $LiPtSe_2$, $MgPdS_2$, $MgPtS_2$, and $MgPtSe_2$ each structurally relaxed from the H-phase into a structure that does not resemble that of a layered TMDC, and so these have also not been included. For others, geometric relaxation transformed the intercalated structure from the H-phase into the T-phase, and so a quantitative comparison between the two structures was not able to be made, though we are able to comment that the T-phase is lower in energy than the H-phase. As such, these points, which included $LiIrS_2$, $MgGeSe_2$, $MgRhS_2$, $MgIrS_2$, and $MgRhSe_2$, have been omitted from Figure 2 in the main article.

F. Intercalation Sites

Here, we present the results of the investigation into the lithium and magnesium intercalation sites within a TMDC vdW gap. The intercalation sites typically considered for the study of intercalation into layered TMDC materials are the octahedrally coordinated site above the metal atom, and the tetragonally coordinated site above the chalcogen atom. In

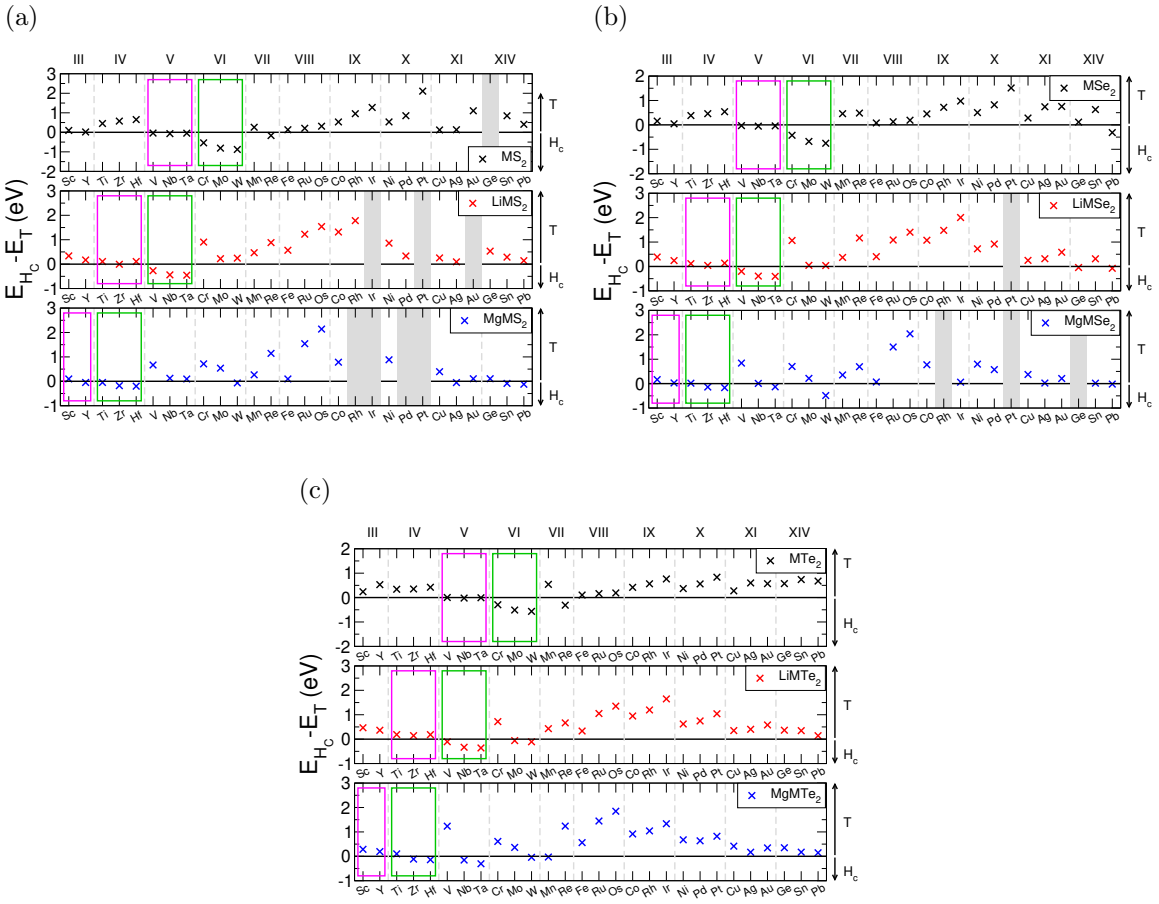

Figure S 4: Comparison of the TMDC T- and Hc-phase energies in the pristine bulk and intercalated forms, for the sulfides (S4a), selenides (S4b), and tellurides (S4c). Positive values indicate a more favourable T-phase, whereas negative values indicate a more favourable Hc-phase. Group V-like behaviour is tracked with the magenta boxes, and Group VI-like behaviour is tracked with the green boxes.

Figure S5 we present the comparison in energy between these two intercalation sites using $E_{\text{Tet}} - E_{\text{Oct}}$. Positive values indicate that the octahedral site is higher in energy than the tetrahedral, and negative values indicate the tetrahedral is lower in energy. For most materials, it is clear to see that the octahedral site is preferred for both intercalants considered. For lithium intercalation, the octahedral is lower in energy by $\sim$0.4 eV, and for magnesium intercalation this is increased to values $\sim$0.6 eV. We attribute this to the larger coordination of the octahedral site being able to better accommodate the double valency of the magnesium intercalant.

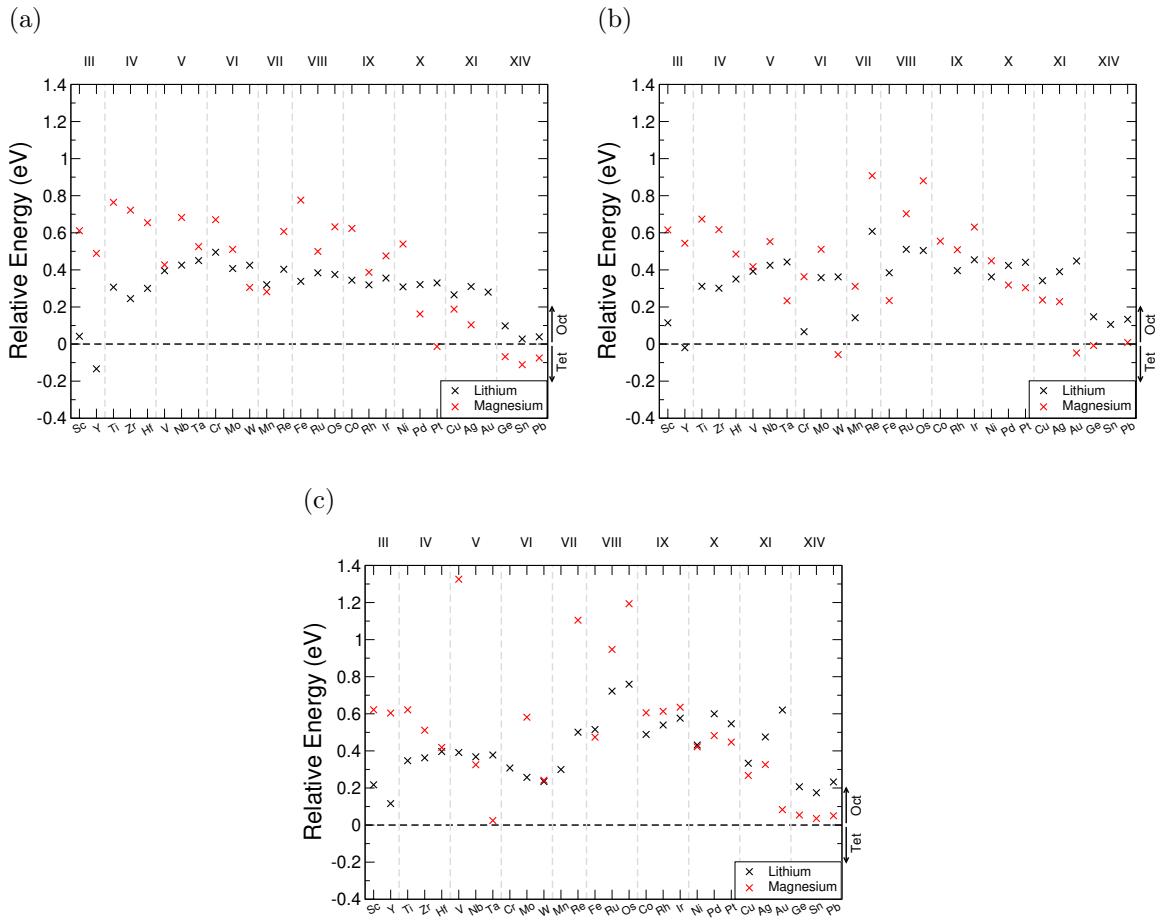

Figure S 5: Relative energy of the tetrahedral intercalation site compared to the octahedral intercalation site for the sulfides (S5a), selenides (S5b), and tellurides (S5c). Data for lithium intercalation is presented in black, and data for magnesium intercalation is presented in red.

A selection of materials do show a favourability for the tetrahedral site. These exceptions, such as $LiYS_2$, $LiYSe_2$, $MgWSe_2$, $MgAuSe_2$, and $MgGeSe_2$, were subject to a closer investigation using larger unit cells, which showed a transition in favourability of the two sites: for concentrations of a in Li_aMX_2 and Mg_aMX_2 greater than 0.5 the tetrahedral site is indeed energetically preferred, but for concentrations lower than 0.5 the octahedral is preferred. Thus, if these TMDC materials are intercalated from MX_2, the octahedral site will be occupied first, and promote further filling of octahedral sites as more intercalants are added.

To further confirm the site of intercalation, nudged elastic band (NEB) calculations were

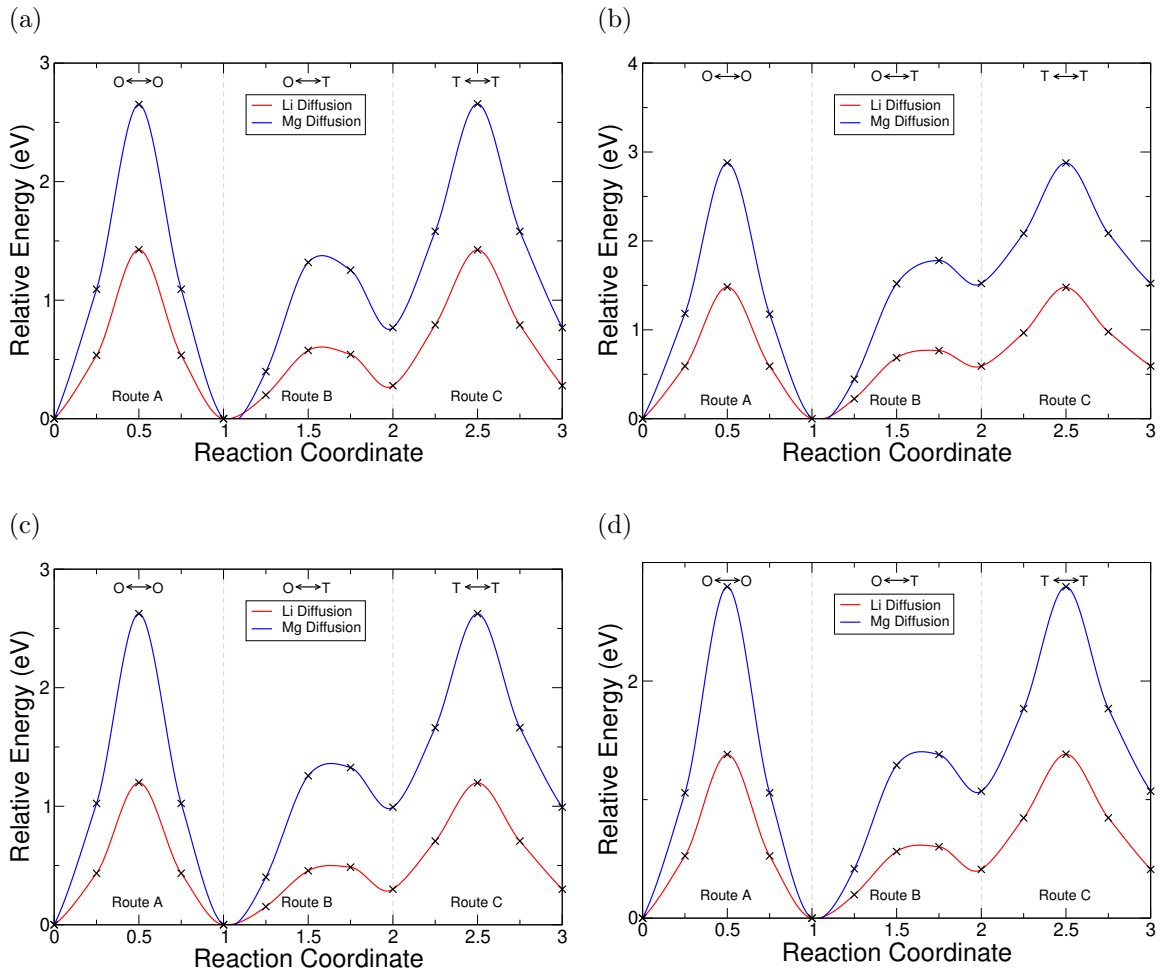

Figure S 6: Nudged elastic band diffusion barriers for ScS_2 (S6a), TiS_2 (S6b), ZrS_2 (S6c), and $ZrSe_2$ (S6d). Octahedral (O) and tetrahedral (T) sites are indicated. Data for lithium diffusion is shown in red, and in blue for magnesium intercalation.

performed along three different routes between two unique intercalation sites, see Figure 3c in the main article. The available intercalation sites are the octahedrally coordinated site above the metal atom, labelled O, and the tetragonally coordinated site above the chalcogen atom, labelled T. We have considered a selection of TMDC materials (ScS_2, TiS_2, ZrS_2, $ZrSe_2$, $ZrTe_2$, HfS_2, SnS_2, and $SnSe_2$) for investigation of possible intercalation routes within a vdW gap, using the nudged elastic band method. We have considered diffusion between two equivalent octahedrally-coordinated (O) sites (Route A), between adjacent octahedrally-coordinated and tetrahedrally-coordinated (T) sites (Route B) and between two equivalent tetrahedrally-coordinated sites (Route C). For both lithium and magnesium

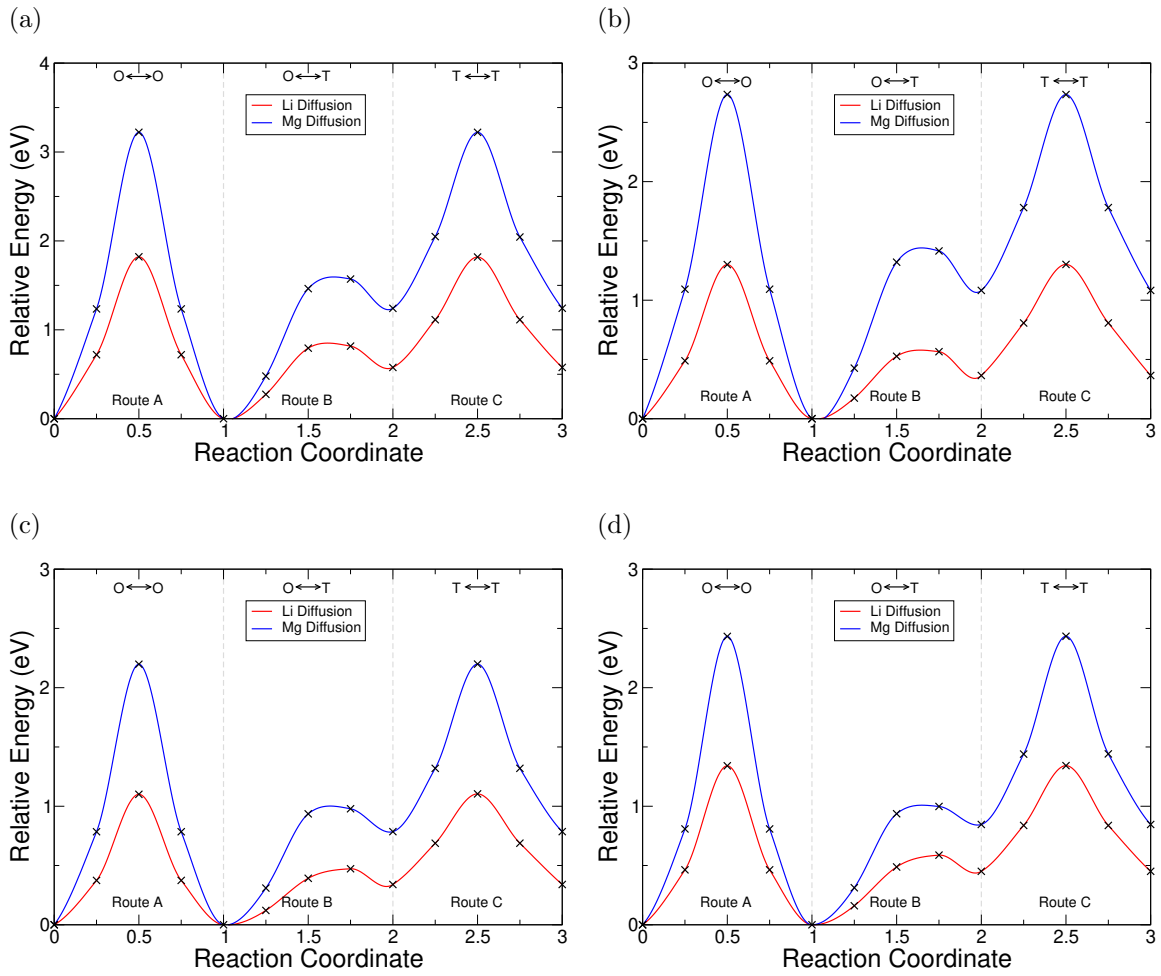

Figure S 7: Nudged elastic band diffusion barriers for $ZrTe_2$ (S7a), HfS_2 (S7b), SnS_2 (S7c), and $SnSe_2$ (S7d). Octahedral (O) and tetrahedral (T) sites are indicated. Data for lithium diffusion is shown in red, and in blue for magnesium intercalation.

intercalation, we find that the octahedrally- and tetrahedrally-coordinated sites commonly used for investigations of intercalated TMDCs are local minima within the layer, and find no other minima. As such, these are the only candidates for intercalation sites. Each of the materials also show that the octahedrally-coordinated site is lower in energy that the tetrahedral, due to a higher Li-S coordination and a larger volume for intercalation[11]. Hence, we conclude that the octahedral is the site is the correct site for ion intercalation, which is in agreement with other TMDC investigations[10–13].

These NEB results also allow us to comment on the diffusion properties of intercalants in such layered materials. As the rate of diffusion is determined through an Arrhenius

equation, the height of the activation barriers is a key parameter for characterizing electrode materials. For each of the materials considered, we see that, whilst Route A offers the most direct path between two octahedral sites, diffusion along Route B has a lower activation energy. Magnesium diffusion is subject to higher barriers. Again, this can be attributed to the higher ionic charge: the larger positive charge of the intercalant and the larger negative charge of the host chalcogen produce stronger Coulombic interactions than those for lithium intercalation. Separation of these oppositely-charged species throughout diffusion therefore requires more energy, and thus a larger barrier to diffusion.

We have not performed an exhaustive investigation into the diffusion barriers of every TMDC material due to the dependency of results on the calculation details. Due to the periodic boundary conditions used here, we have here fixed the positions of the host transition metal atoms throughout the NEB calculation, as the diffusion of a single ion should only cause local distortions and not cause the macroscopic expansion of whole TMDC sheets. Restriction of the out-of-plane expansion results in the barriers we have determined being over-estimations[14]. As such, our use of the NEB is focused on determination of intercalation site.

II. TMDC DATA

In the following sections, we shall present further results that supplement the discussions in the main article. Unless otherwise stated, these will be for the T-phase materials.

A. Bader Charge Analysis

In the main article, we presented the Bader charges of the ions in the intercalated sulfide structures. In Figure S8, we also present the equivalent results for the selenide and telluride structures. We also include in Table SIII, Table SIV, and Table SV the numerical values of the charges for the sulfide, selenide, and telluride structures, respectively.

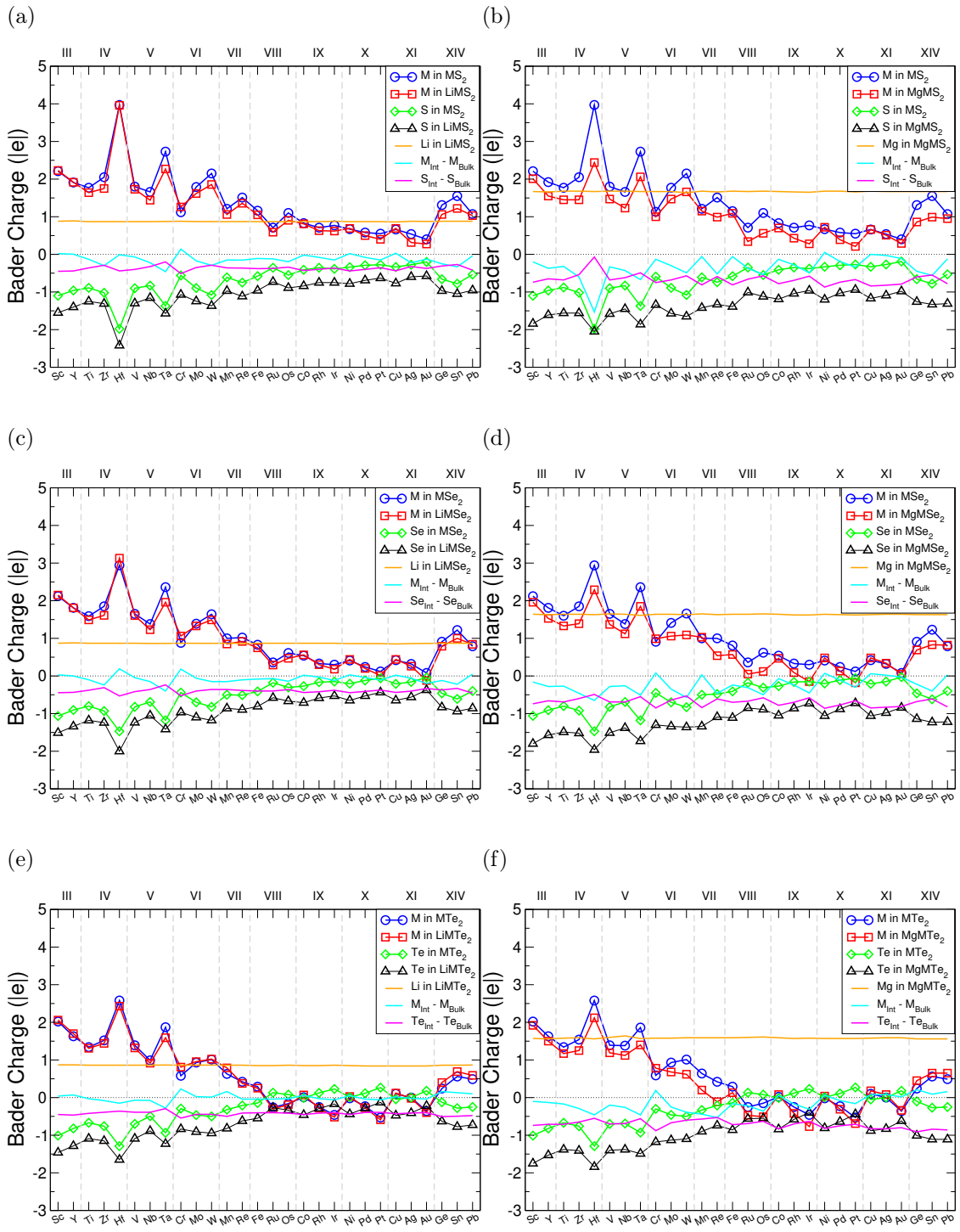

Figure S 8: Bader charges for the metal, chalcogen, lithium, and magnesium atoms in the bulk, $LiMX_2$, and $MgMX_2$ structures. Sulfide data is presented in S8a and S8b, selenide data is presented in S8c and S8d, and telluride data is presented in S8e and S8f.

	Pristine MX_2 Charges (|e|)		Intercalated $LiMX_2$ Charges (|e|)			Intercalated $MgMX_2$ Charges (|e|)		
TMDC	M	X	M	X	Li	M	X	Mg
ScS_2	2.21	-1.10	2.23	-1.55	0.88	2.01	-1.84	1.67
YS_2	1.92	-0.96	1.92	-1.40	0.89	1.55	-1.61	1.66
TiS_2	1.77	-0.89	1.64	-1.25	0.87	1.45	-1.56	1.68
ZrS_2	2.05	-1.02	1.75	-1.31	0.87	1.45	-1.56	1.68
HfS_2	3.97	-1.98	3.96	-2.42	0.87	2.44	-2.05	1.67
VS_2	1.80	-0.90	1.73	-1.30	0.87	1.47	-1.58	1.68
NbS_2	1.66	-0.83	1.44	-1.16	0.87	1.23	-1.45	1.68
TaS_2	2.73	-1.37	2.27	-1.57	0.88	2.06	-1.86	1.67
CrS_2	1.12	-0.56	1.26	-1.07	0.88	1.00	-1.34	1.67
MoS_2	1.79	-0.90	1.62	-1.25	0.87	1.47	-1.57	1.67
WS_2	2.15	-1.08	1.86	-1.37	0.87	1.66	-1.65	1.64
MnS_2	1.21	-0.61	1.06	-0.97	0.87	1.15	-1.42	1.68
ReS_2	1.51	-0.75	1.36	-1.12	0.87	0.99	-1.33	1.66
FeS_2	1.16	-0.58	1.05	-0.96	0.87	1.09	-1.39	1.68
RuS_2	0.71	-0.36	0.59	-0.73	0.87	0.34	-1.01	1.67
OsS_2	1.10	-0.55	0.91	-0.89	0.87	0.56	-1.12	1.68
CoS_2	0.83	-0.41	0.81	-0.84	0.87	0.70	-1.19	1.67
RhS_2	0.71	-0.36	0.63	-0.75	0.87	0.43	-1.04	1.66
IrS_2	0.77	-0.39	0.62	-0.75	0.88	0.28	-0.96	1.65
NiS_2	0.67	-0.34	0.69	-0.78	0.87	0.72	-1.20	1.68
PdS_2	0.58	-0.29	0.50	-0.69	0.87	0.39	-1.03	1.68
PtS_2	0.55	-0.28	0.40	-0.63	0.87	0.21	-0.94	1.66
CuS_2	0.66	-0.34	0.69	-0.77	0.86	0.66	-1.17	1.68
AgS_2	0.54	-0.28	0.32	-0.60	0.88	0.51	-1.09	1.67
AuS_2	0.40	-0.20	0.28	-0.57	0.88	0.29	-0.98	1.67
GeS_2	1.31	-0.66	1.06	-0.97	0.88	0.86	-1.26	1.67
SnS_2	1.55	-0.78	1.22	-1.05	0.88	0.99	-1.33	1.67
PbS_2	1.07	-0.54	1.03	-0.96	0.88	0.95	-1.31	1.67

Table S III: Average Bader charge values for constituent ions in sulfide MS_2, $LiMS_2$, and $MgMS_2$ compounds.

	Pristine MX_2 Charges (|e|)		Intercalated $LiMX_2$ Charges (|e|)			Intercalated $MgMX_2$ Charges (|e|)		
TMDC	M	X	M	X	Li	M	X	Mg
$ScSe_2$	2.12	-1.07	2.15	-1.51	0.87	1.96	-1.80	1.64
YSe_2	1.81	-0.91	1.81	-1.34	0.88	1.53	-1.57	1.63
$TiSe_2$	1.59	-0.80	1.49	-1.18	0.87	1.33	-1.49	1.64
$ZrSe_2$	1.85	-0.93	1.61	-1.24	0.87	1.39	-1.52	1.64
$HfSe_2$	2.94	-1.47	3.13	-2.00	0.87	2.29	-1.96	1.63
VSe_2	1.65	-0.82	1.61	-1.24	0.87	1.37	-1.51	1.65
$NbSe_2$	1.38	-0.69	1.23	-1.05	0.87	1.12	-1.38	1.64
$TaSe_2$	2.36	-1.18	1.96	-1.42	0.87	1.85	-1.73	1.61
$CrSe_2$	0.88	-0.44	1.06	-0.97	0.87	0.99	-1.30	1.64
$MoSe_2$	1.39	-0.70	1.33	-1.10	0.87	1.06	-1.34	1.64
WSe_2	1.64	-0.82	1.49	-1.18	0.87	1.09	-1.36	1.63
$MnSe_2$	1.00	-0.50	0.85	-0.86	0.87	1.03	-1.34	1.65
$ReSe_2$	1.02	-0.51	0.92	-0.90	0.87	0.54	-1.09	1.63
$FeSe_2$	0.83	-0.41	0.75	-0.81	0.87	0.57	-1.11	1.64
$RuSe_2$	0.36	-0.18	0.29	-0.58	0.87	0.05	-0.85	1.64
$OsSe_2$	0.61	-0.31	0.47	-0.67	0.87	0.12	-0.89	1.65
$CoSe_2$	0.54	-0.27	0.56	-0.71	0.87	0.47	-1.05	1.64
$RhSe_2$	0.33	-0.17	0.30	-0.59	0.87	0.09	-0.86	1.62
$IrSe_2$	0.30	-0.15	0.18	-0.53	0.87	-0.15	-0.73	1.62
$NiSe_2$	0.41	-0.21	0.44	-0.65	0.86	0.48	-1.06	1.64
$PdSe_2$	0.24	-0.12	0.20	-0.53	0.86	0.13	-0.88	1.63
$PtSe_2$	0.12	-0.06	0.01	-0.44	0.86	-0.18	-0.72	1.62
$CuSe_2$	0.42	-0.21	0.44	-0.65	0.85	0.48	-1.06	1.63
$AgSe_2$	0.32	-0.16	0.26	-0.56	0.86	0.34	-0.98	1.64
$AuSe_2$	0.08	-0.04	-0.12	-0.37	0.87	0.05	-0.84	1.64
$GeSe_2$	0.91	-0.46	0.79	-0.83	0.87	0.69	-1.14	1.63
$SnSe_2$	1.22	-0.61	1.00	-0.94	0.87	0.83	-1.23	1.63
$PbSe_2$	0.79	-0.40	0.84	-0.86	0.87	0.82	-1.22	1.63

Table S IV: Average Bader charge values for constituent ions in selenide MSe_2, $LiMSe_2$, and $MgMSe_2$ compounds.

	Pristine MX_2 Charges (|e|)		Intercalated $LiMX_2$ Charges (|e|)			Intercalated $MgMX_2$ Charges (|e|)		
TMDC	M	X	M	X	Li	M	X	Mg
$ScTe_2$	2.02	-1.01	2.06	-1.46	0.87	1.92	-1.75	1.57
YTe_2	1.63	-0.82	1.70	-1.29	0.87	1.50	-1.53	1.56
$TiTe_2$	1.34	-0.67	1.31	-1.09	0.86	1.17	-1.38	1.58
$ZrTe_2$	1.52	-0.76	1.44	-1.15	0.86	1.25	-1.41	1.59
$HfTe_2$	2.58	-1.29	2.43	-1.65	0.86	2.12	-1.84	1.56
VTe_2	1.39	-0.70	1.32	-1.09	0.86	1.19	-1.40	1.60
$NbTe_2$	0.99	-0.50	0.91	-0.89	0.87	1.12	-1.38	1.64
$TaTe_2$	1.87	-0.94	1.59	-1.23	0.86	1.40	-1.49	1.57
$CrTe_2$	0.58	-0.29	0.81	-0.84	0.86	0.78	-1.18	1.58
$MoTe_2$	0.93	-0.47	0.96	-0.91	0.86	0.68	-1.13	1.58
WTe_2	1.01	-0.50	1.02	-0.95	0.86	0.62	-1.10	1.59
$MnTe_2$	0.63	-0.32	0.79	-0.82	0.86	0.20	-0.90	1.59
$ReTe_2$	0.42	-0.21	0.38	-0.62	0.86	-0.11	-0.74	1.59
$FeTe_2$	0.29	-0.15	0.25	-0.55	0.85	0.13	-0.86	1.59
$RuTe_2$	-0.26	0.13	-0.30	-0.27	0.85	-0.47	-0.56	1.60
$OsTe_2$	-0.16	0.08	-0.19	-0.33	0.86	-0.51	-0.55	1.61
$CoTe_2$	0.01	-0.01	0.07	-0.46	0.85	0.08	-0.84	1.59
$RhTe_2$	-0.25	0.13	-0.28	-0.29	0.85	-0.42	-0.58	1.57
$IrTe_2$	-0.46	0.23	-0.52	-0.17	0.86	-0.77	-0.40	1.58
$NiTe_2$	-0.02	0.01	0.03	-0.44	0.85	0.04	-0.81	1.57
$PdTe_2$	-0.23	0.12	-0.27	-0.28	0.84	-0.31	-0.64	1.57
$PtTe_2$	-0.53	0.27	-0.59	-0.13	0.84	-0.69	-0.44	1.57
$CuTe_2$	0.10	-0.05	0.12	-0.48	0.84	0.18	-0.88	1.58
$AgTe_2$	0.00	0.00	-0.02	-0.41	0.84	0.08	-0.83	1.59
$AuTe_2$	-0.36	0.18	-0.40	-0.22	0.84	-0.34	-0.62	1.59
$GeTe_2$	0.24	-0.13	0.40	-0.63	0.86	0.45	-1.01	1.56
$SnTe_2$	0.56	-0.28	0.69	-0.78	0.86	0.65	-1.11	1.56
$PbTe_2$	0.49	-0.25	0.59	-0.73	0.87	0.65	-1.11	1.56

Table S V: Average Bader charge values for constituent ions in telluride MTe_2, $LiMTe_2$, and $MgMTe_2$ compounds.

B. Intermediate Bader Charges

Above, and in the main article, we have only considered the Bader charges of the extremes of intercalation (the MX_2, $LiMX_2$, and $MgMX_2$ compositions). Of course, during cycling of a cell, intermediate concentrations will be achieved, potentially resulting in different charges on the component ions to those at each end of the intercalation range. To investigate the charges each ionic species can explore, we present in Figure S9 and Figure S10 the charges exhibited by ions in selected TMDCs, across each of the 24 intercalant configurations considered in this work. Straight-line connections between the MX_2 and $LiMX_2$/$MgMX_2$ compositions have been included as visual aid.

We present the results for the intercalated ZrX_2 materials in Figure S9, and for NbS_2, GeS_2, and SnS_2 in Figure S10. The first thing of note is the uniform charge exhibited by both lithium and magnesium intercalants. This follows the constant charge exhibited by both intercalants regardless of which host material they are introduced to. Of the TMDCs considered, the transition metals all closely follow the linear trend suggested, with very little spread. On the other hand, the chalcogens follow the linear line fairly well but present a much larger spread in charges.

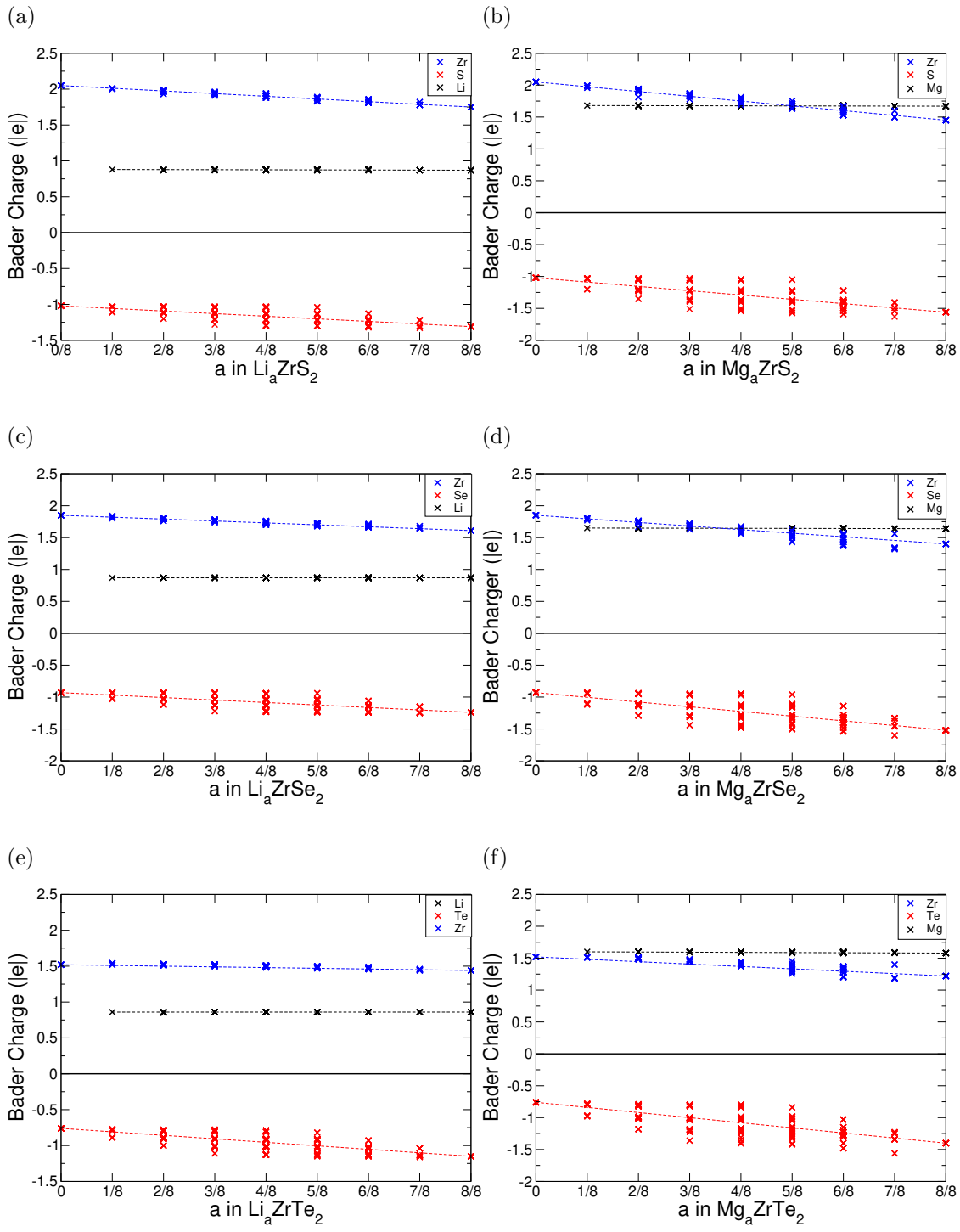

Figure S 9: Bader charges for lithium-intercalated ZrS_2 (S9a), $ZrSe_2$ (S9c), and $ZrTe_2$ (S9e) across the different intercalant concentrations and configurations considered. Similarly, the Bader charges of magnesium-intercalated ZrS_2 (S9b), $ZrSe_2$ (S9d), and $ZrTe_2$ (S9f) are also shown. Dashed lines connecting the initial and final charges have also been included as visual aid.

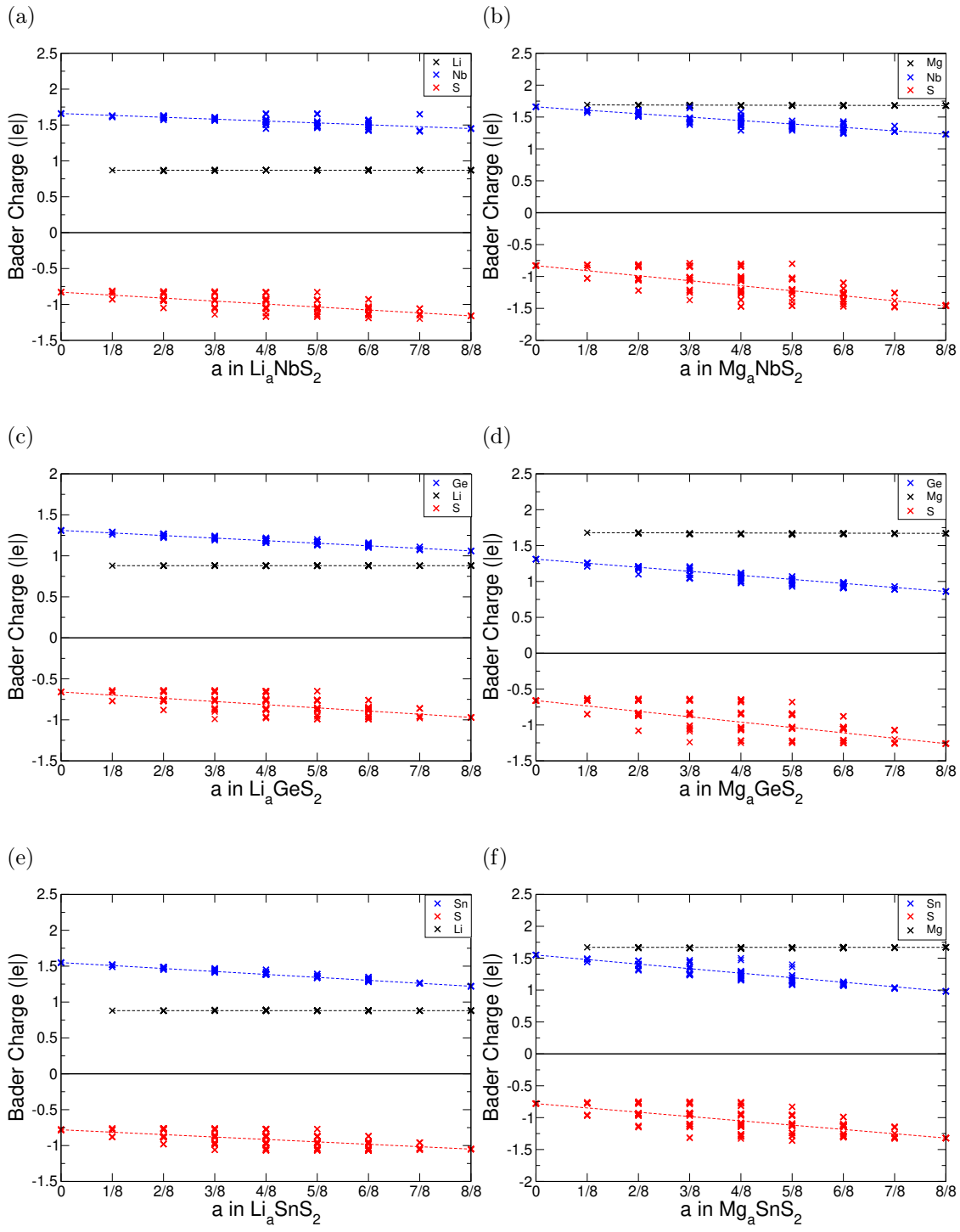

Figure S 10: Bader charges for lithium-intercalated NbS_2 (S10a), GeS_2 (S10c), and SnS_2 (S10e) across the different intercalant concentrations and configurations considered. Similarly, the Bader charges of magnesium-intercalated NbS_2 (S10b), GeS_2 (S10d), and SnS_2 (S10f) are also shown. Dashed lines connecting the initial and final charges have also been included as visual aid.

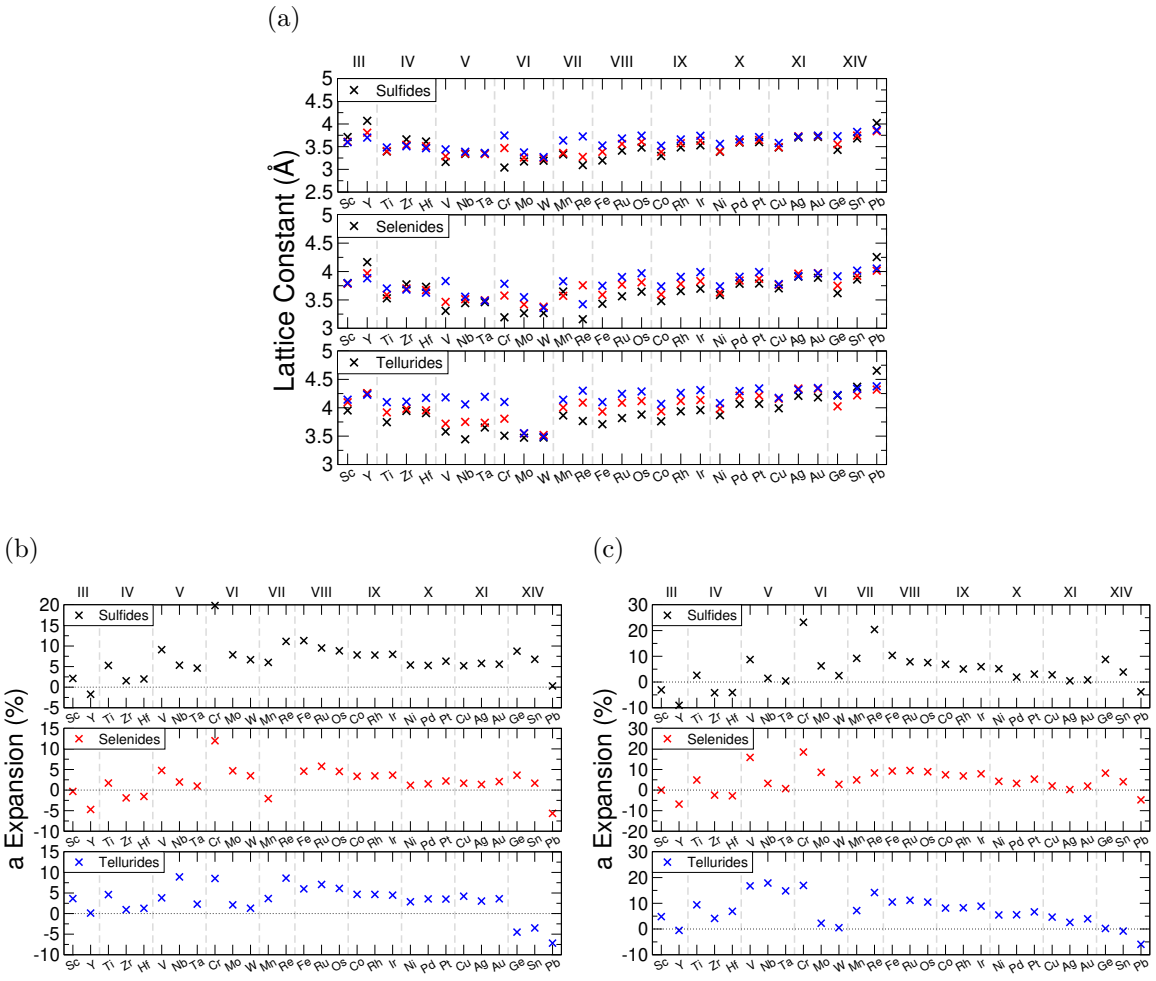

Figure S 11: In-plane lattice constants for the pristine (black), lithium-intercalated (red), and magnesium-intercalated (blue) TMDCs. Sulfide data is presented in the top, selenide data is presented in the middle, and telluride data is presented in the bottom. The percentage expansion is then presented in S11b for lithium intercalation, and in S11c for magneisum intercalation.

C. Geometry - Lattice

In Figure S11a we present the in-plane lattice constants for the pristine (black), lithium-intercalated (red), and magnesium-intercalated (blue) structures. In general, we see an increase of the in-plane lattice constant with intercalation. This is emphasised in Figures S11b and S11c, where we show the resultant percentage expansion of the in-plane lattice constant due to lithium (S11b) and magnesium (S11c) intercalation. There is a larger percentage expansion for TMDCs composed of transition metals from Period IV, but this

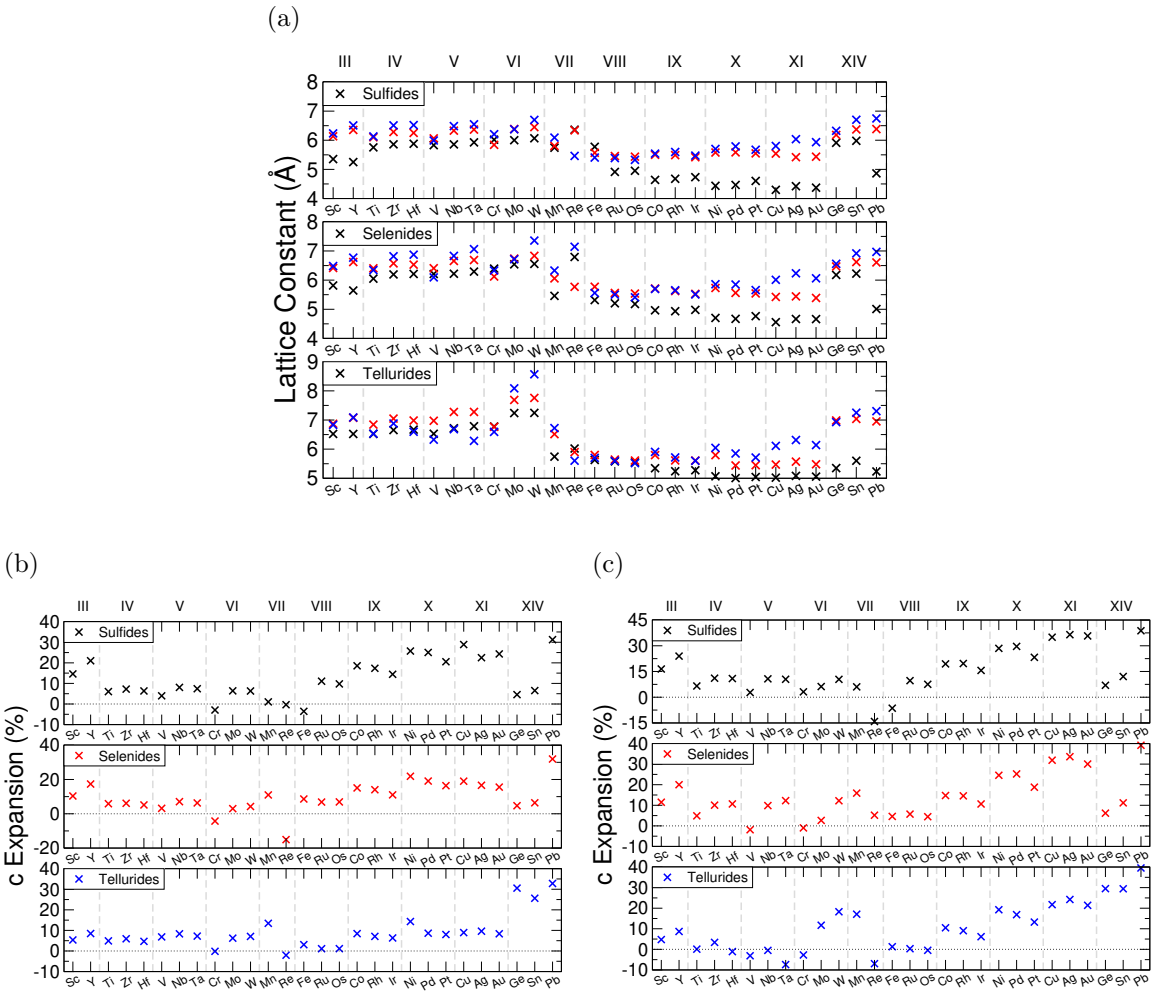

Figure S 12: Out-of-plane lattice constants for the pristine (black), lithium-intercalated (red), and magnesium-intercalated (blue) TMDCs. Sulfide data is presented in the top, selenide data is presented in the middle, and telluride data is presented in the bottom. The percentage expansion is then presented in S12b for lithium intercalation, and in S12c for magnesium intercalation.

is simply due to the smaller initial lattice constant of the unintercalated structures. For lithium intercalation, most of the TMDCs exhibit in-plane lattice expansion of 5-10%, and there are larger expansions under intercalation with magnesium. Somewhat surprisingly, we identify a contraction of the sulfides and selenides paired with Group IV and V metals. Overall, however, we show that most of these materials demonstrate in-plane expansions within ±10%, which is ideal for electrode applications.

As intercalation into the vdW gap changes the nature of the out-of-plane bonding, changes

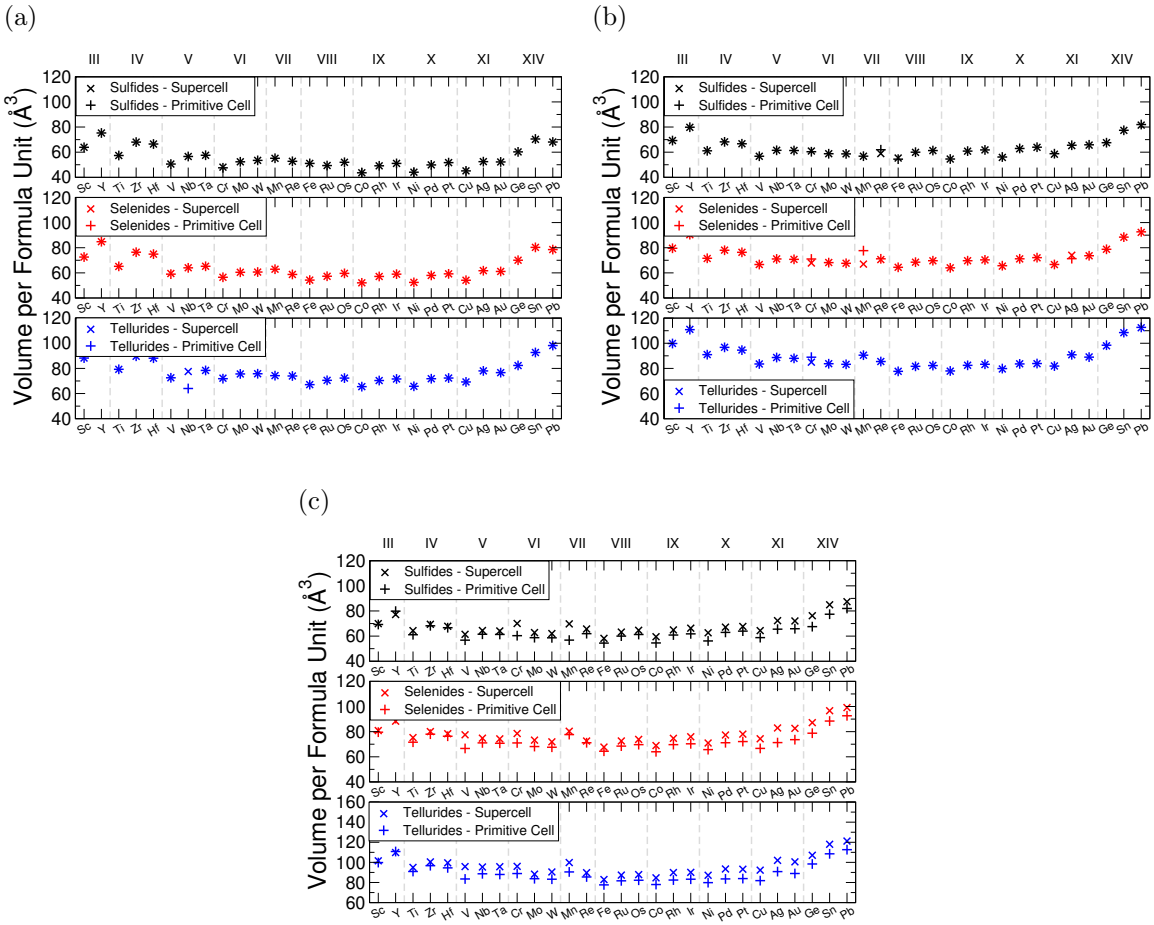

Figure S 13: Volumes of pristine (S13a), lithium-intercalated (S13b) and magnesium-intercalated (S13c) TMDCs In each of these, sulfide data is presented in black (top), selenide data is presented in red (middle), and telluride data is presented in blue (bottom).

to the out-of-plane lattice constant can be expected. We present in Figure S12a the out-of-plane lattice constants for the pristine (black), lithium-intercalated (red), and magnesium-intercalated (blue) structures. For TMDC sulfides, and materials composed of transition metals in Groups III to VII, and XIV, we see a large expansion ($\sim$20%) of the lattice constant with intercalation. However, for transition metals in Groups VIII to XI there is either a very small ($<$5%) expansion or a contraction of the out-of-plane lattice. We indicate this with the percentage expansions in Figure S12b (lithium intercalation) and in Figure S12c (magnesium intercalation).

In Figure S13, we then present the formula unit volumes of the pristine (Figure S13a),

lithium-intercalated (Figure S13b), and magnesium-intercalated (Figure S13c) structures. We have included the volumes for the primitive and supercell ($2\times2\times2$), used for determining the volumetric expansion presented in the main article.

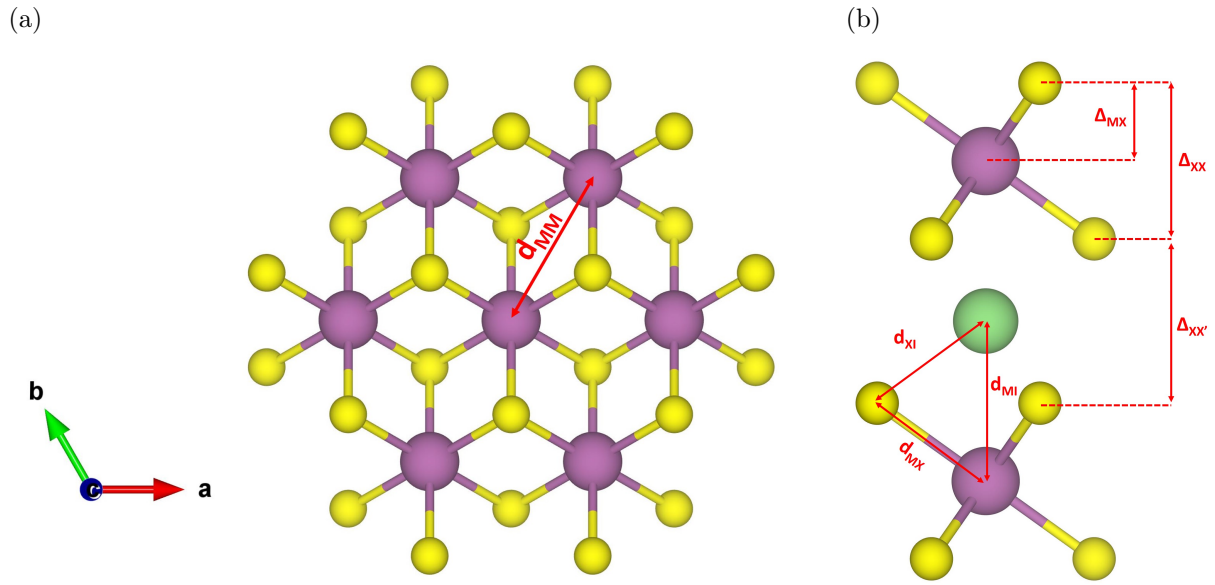

Figure S 14: Labels used for discussions of TMDC geometry. S14a shows a 'top-down' view of the TMDC basal plane, and S14b shows a side-view of the TMDC structure.

D. Geometry - Ions

We indicate our labelling of the different ionic distances for the following discussion in Figure S14. This includes the in-plane metal-metal distance (d_{MM}), the bond length/distance between the host transition metal and the chalcogen (d_{MX}), the bond length/distance between the host chalcogen of the host and the intercalant species (d_{XI}), and the distance between the host transition metal and the intercalant (d_{MI}). We also consider the vertical separation of the host transition metal and chalcogen (Δ_{MX}), the vertical separation between chalcogen atoms on opposing sides of a TMDC sheet (Δ_{XX}), and the vertical separation between chalcogen species on opposing sides of the vdW gap ($\Delta_{XX'}$).

Above, we commented on a general expansion of the in-plane lattice constant under intercalation. This leads to an increase in the distance between transition metal atoms within a layer of the host TMDC material, as is shown in Figure S15a. The exceptions to this are the sulfide and selenide materials composed of Group IV and V metals, which demonstrated a small contraction of the in-plane structure, and here show a shortening of the M-M distance.

The distances between the host transition metal and chalcogen ions are shown in Fig-

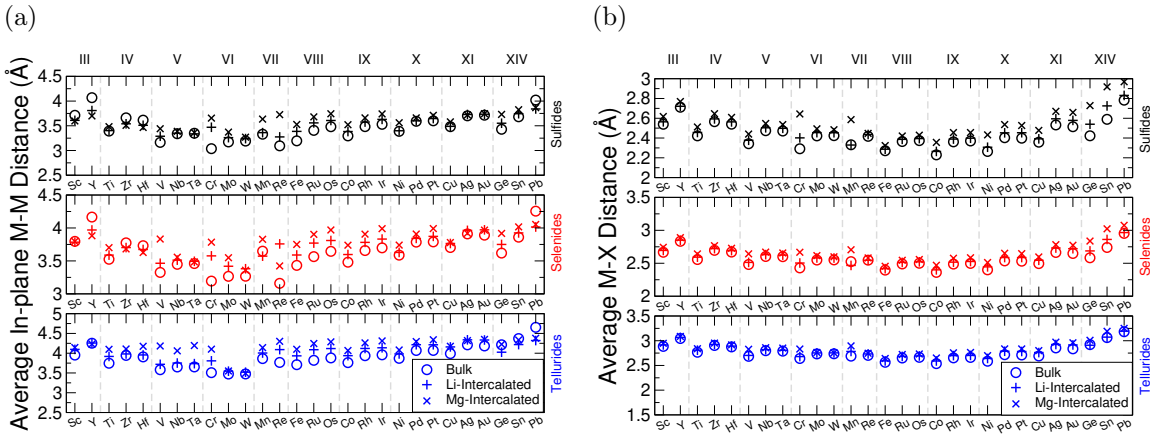

Figure S 15: Characteristic distances of the host TMDC materials. S15a presents the values of d_{MM}, and S15b presents the values of d_{MX}. The sulfides (top), selenides (middle), and telluride (bottom) materials are included, with the results for the pristine bulk structures presented with circles, lithium-intercalated presented with pluses, and magnesium-intercalated presented with crosses.

ure S15b. We identify a slight lengthening of the metal-chalcogen bond length when an intercalant is introduced to the TMDC structure. We attribute this to the significant charge donation from the intercalant to the host material, and a Coulombic attraction between the chalcogen and intercalant species. For the selenide and telluride materials in particular, the M-X bond length is approximately the same with both lithium and magnesium intercalation.

Above, we saw the general expansion of the **c** lattice vector with intercalation, and here aim to offer some insight into this expansion. In Figure S16a we show the vertical separation between chalcogen species on opposing sides of the vdW spacing ($\Delta_{XX'}$). This gives an indication of the separation between consecutive TMDC layers, where we see a clear increase in this separation (with the exception of the Cr, Mn, Re, Ge, and Sn materials, for which there is little change). The expansion is to be expected from the introduction of an intercalant as it dramatically changes the nature of the out-of-plane bonding.

We similarly show in Figure S16b the vertical separation between intralayer chalcogen species of the same TMDC sheet but on opposing basal planes (Δ_{XX}): This gives a measure of the thickness of each TMDC sheet. Groups III-IV, X-XI, and XIV all show a vertical stretching of the TMDC layer with intercalation, with magnesium intercalation resulting in a greater stretching than lithium intercalation. Groups V and VI show a mixture of expansion

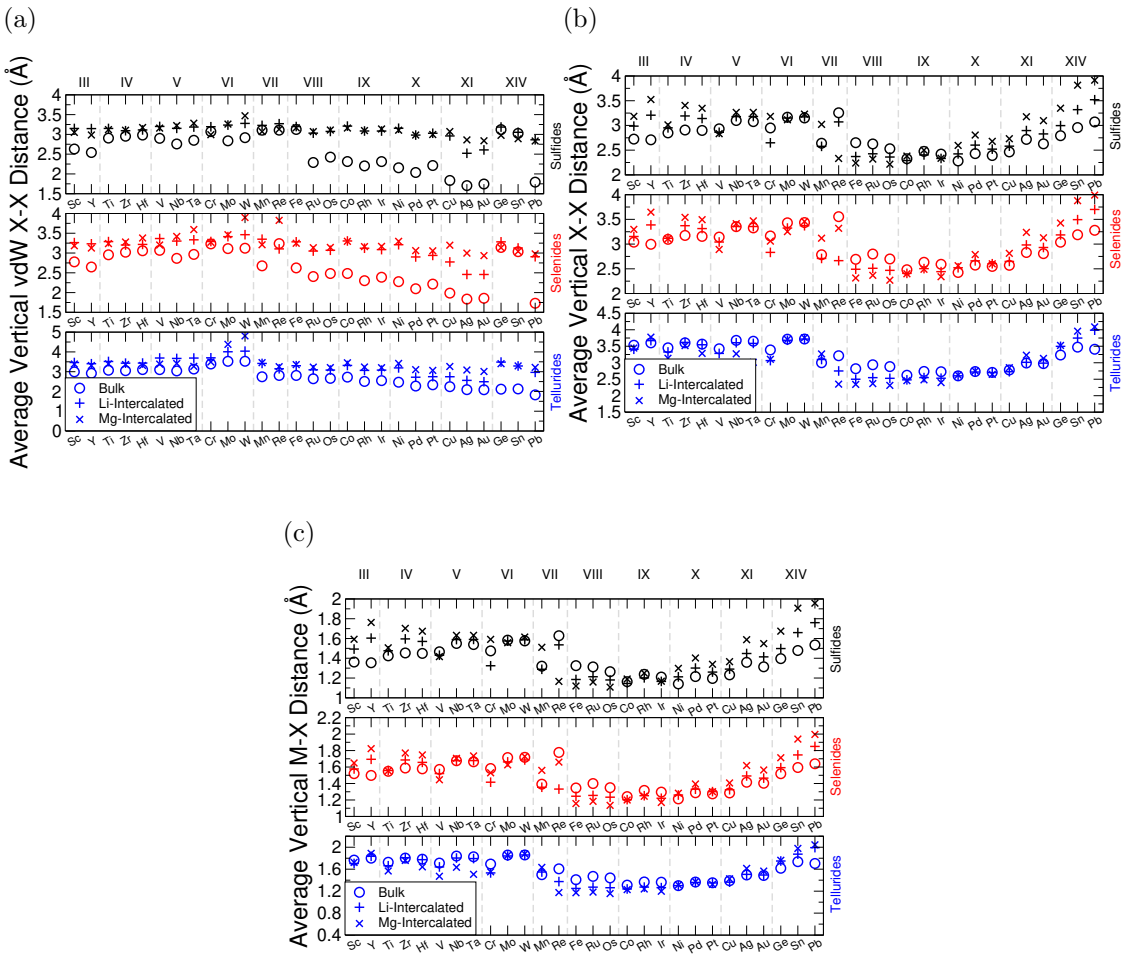

Figure S 16: Characteristic distances of the host TMDC materials. S16c presents the values of Δ_{MX}, S16b presents the values of Δ_{XX}, and S16a presents the values of $\Delta_{XX'}$. The sulfides (top), selenides (middle), and telluride (bottom) materials are included, with the results for the pristine bulk structures presented with circles, lithium-intercalated presented with pluses, and magnesium-intercalated presented with crosses.

and contraction. Groups VII-IX, finally, show a contraction, with magnesium intercalation again showing the most dramatic change.

A closer look at the M-X bonding is revealed in Figure S16c, where we show the vertical separation between the metal atom and its nearest six coordinated chalcogens. This is another useful descriptor for the thickness of a TMDC layer. We identify the same trends with Δ_{MX} as we did for Δ_{XX}, with Groups III-IV, X-XI, and XIV all show a vertical stretching of the TMDC layer with intercalation, with magnesium intercalation resulting in a greater

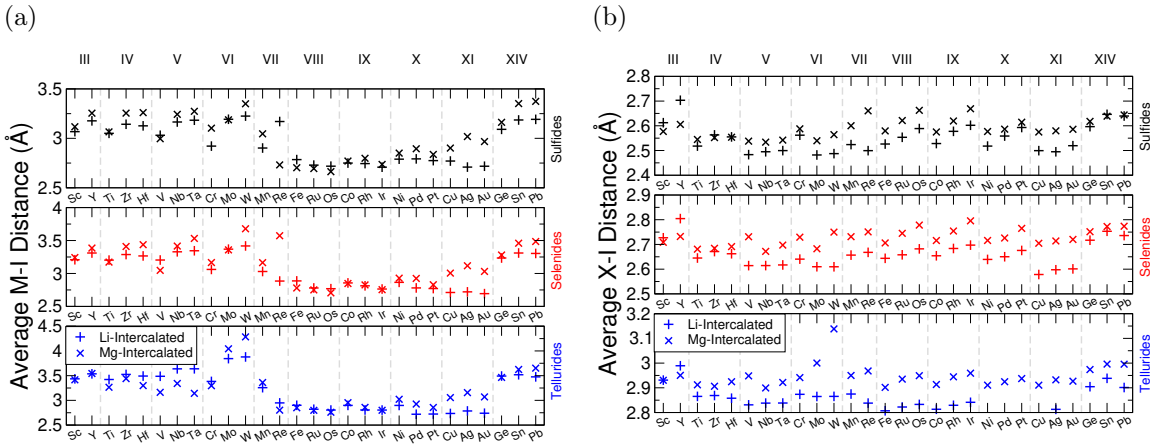

Figure S 17: Characteristic distances of the intercalated TMDC materials. S17a presents the values of d_{MI}, and S17b presents the values of d_{XI}. The sulfides (top), selenides (middle), and telluride (bottom) materials are included, with the results for lithium-intercalated structures presented with pluses, and magnesium-intercalated presented with crosses.

stretching than lithium intercalation; Groups V and VI show a mixture of expansion and contraction; and Groups VII-IX show a contraction. In each of these, magnesium intercalation again results in the most dramatic changes to the structure. We also note the more significant effect the intercalant has on the sulfides compared with heavier chalcogens. In particular, the Group III, IV, X, XI, and XIV tellurides all show minimal changes to Δ_{MX} which are pronounced in the case of the sulfides. Whilst we saw a very uniform changes to the length of the M-X bond (as was discussed above in Figure S15b), there is a much more varied behaviour for the vertical separation between the M and X species. This results in a wide range of bonding angles.

In Figure S17 we show the distances between the host transition metal and the intercalant (Figure S17a), d_{MI}, and the distance between the intercalant and the nearest six chalcogens of the host material (Figure S17b), d_{XI}.

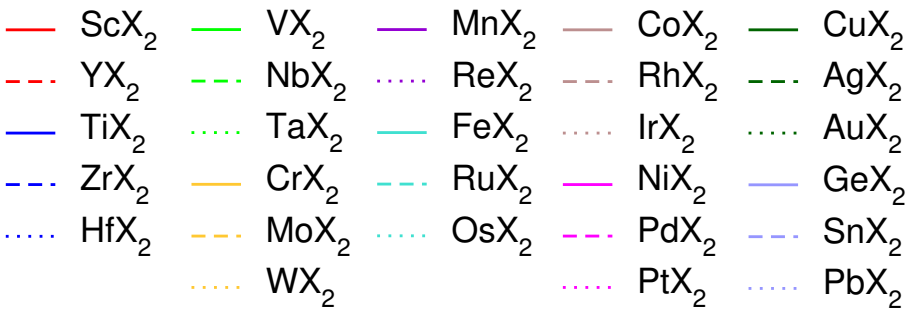

Figure S 18: Legend used for following figures. Transition metals within the same Group have been coloured the same. Solid lines correspond to Period IV, dashed lines correspond to Period V, and dotted lines correspond to Period VI transition metals. Figures requiring this legend include Figure S19, Figure S20, Figure S21, and Figure S28.

E. Voltages

In the main article, we presented the average voltages for each of the sulfide TMDCs, and only for selected TMDCs were the full voltage profiles shown. Here, we present the average voltages and the full voltage profiles for each of the TMDCs.

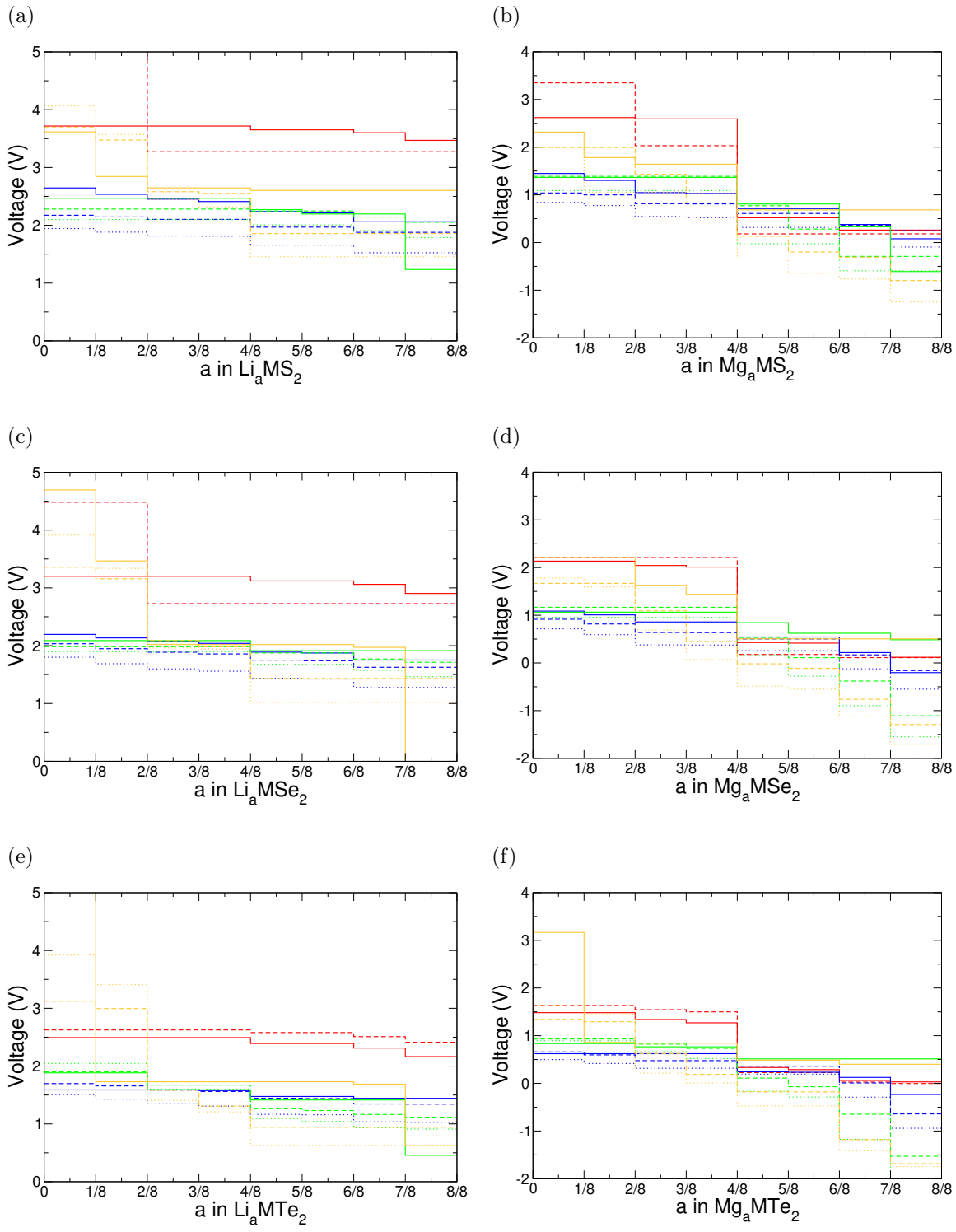

Figure S 19: Intercalation voltage profiles for Group III-VI TMDCs. Data for sulfide materials is given in S19a and S19b, selenide materials is given in S19c and S19d, and telluride materials is given in S19e and S19f. Full legend is given in Figure S18.

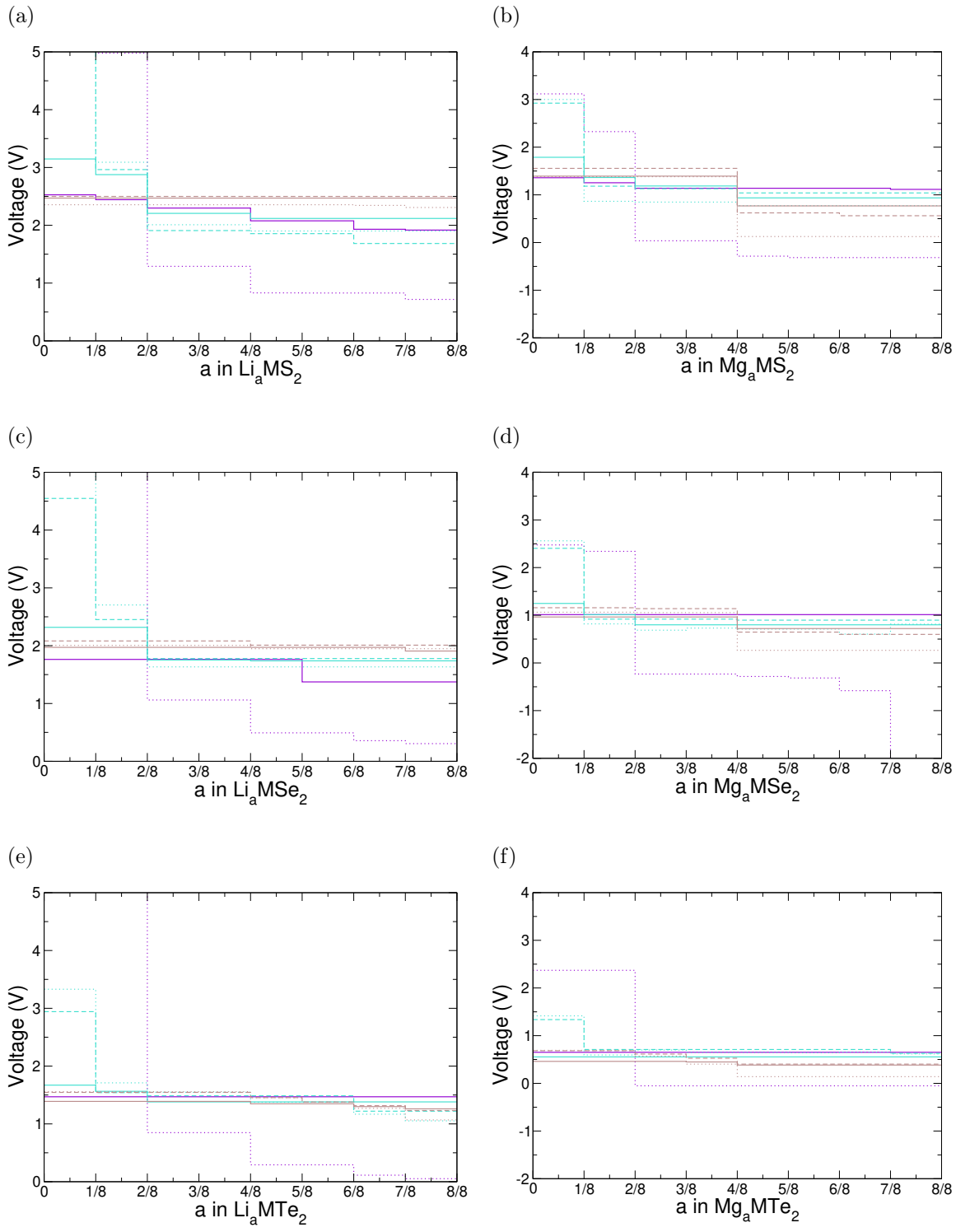

Figure S 20: Intercalation voltage profiles for Group VII-IX TMDCs. Data for sulfide materials is given in S20a and S20b, selenide materials is given in S20c and S20d, and telluride materials is given in S20e and S20f. Full legend is given in Figure S18.

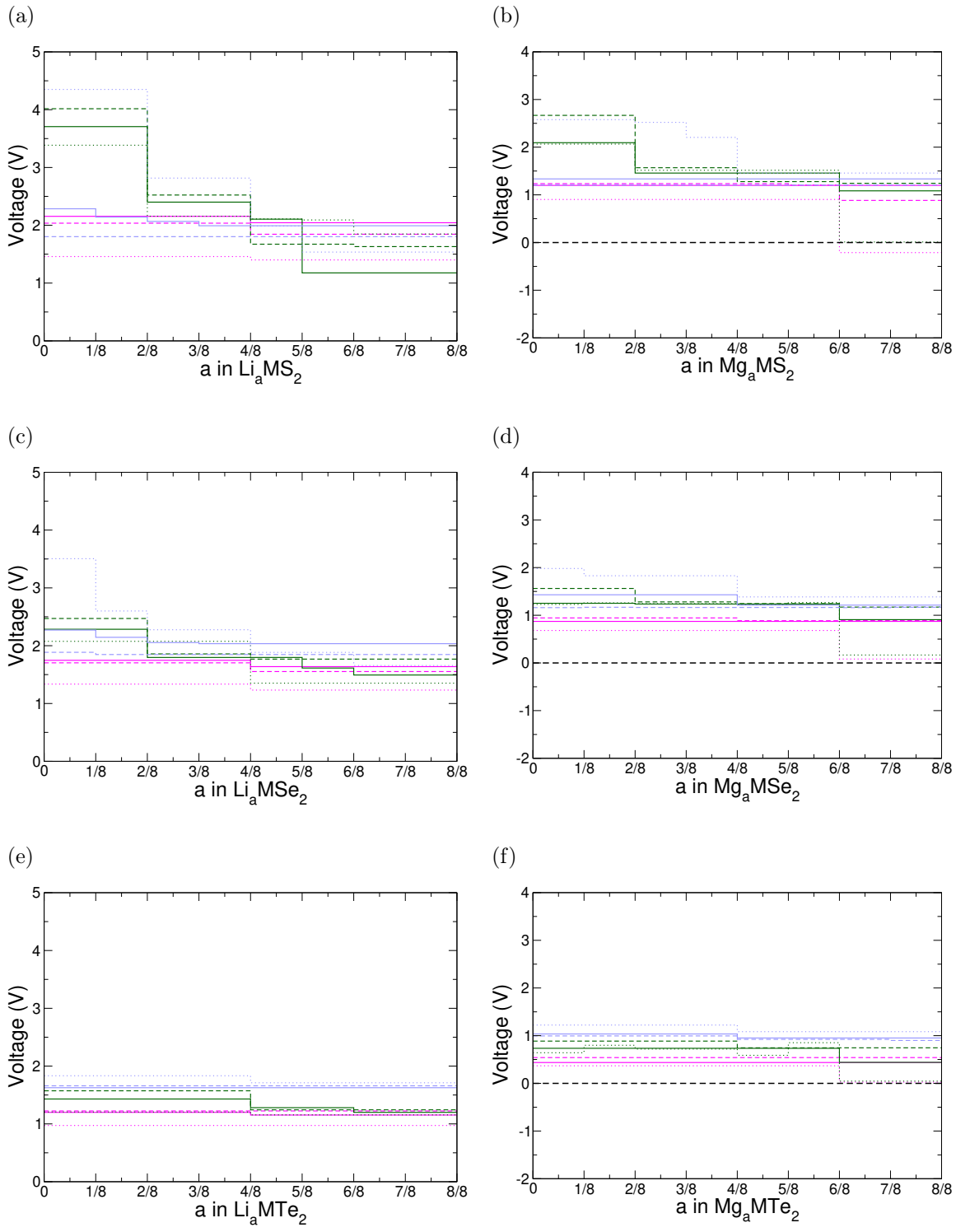

Figure S 21: Intercalation voltage profiles for Group X-XIV TMDCs. Data for sulfide materials is given in S21a and S21b, selenide materials is given in S21c and S21d, and telluride materials is given in S21e and S21f. Full legend is given in Figure S18.

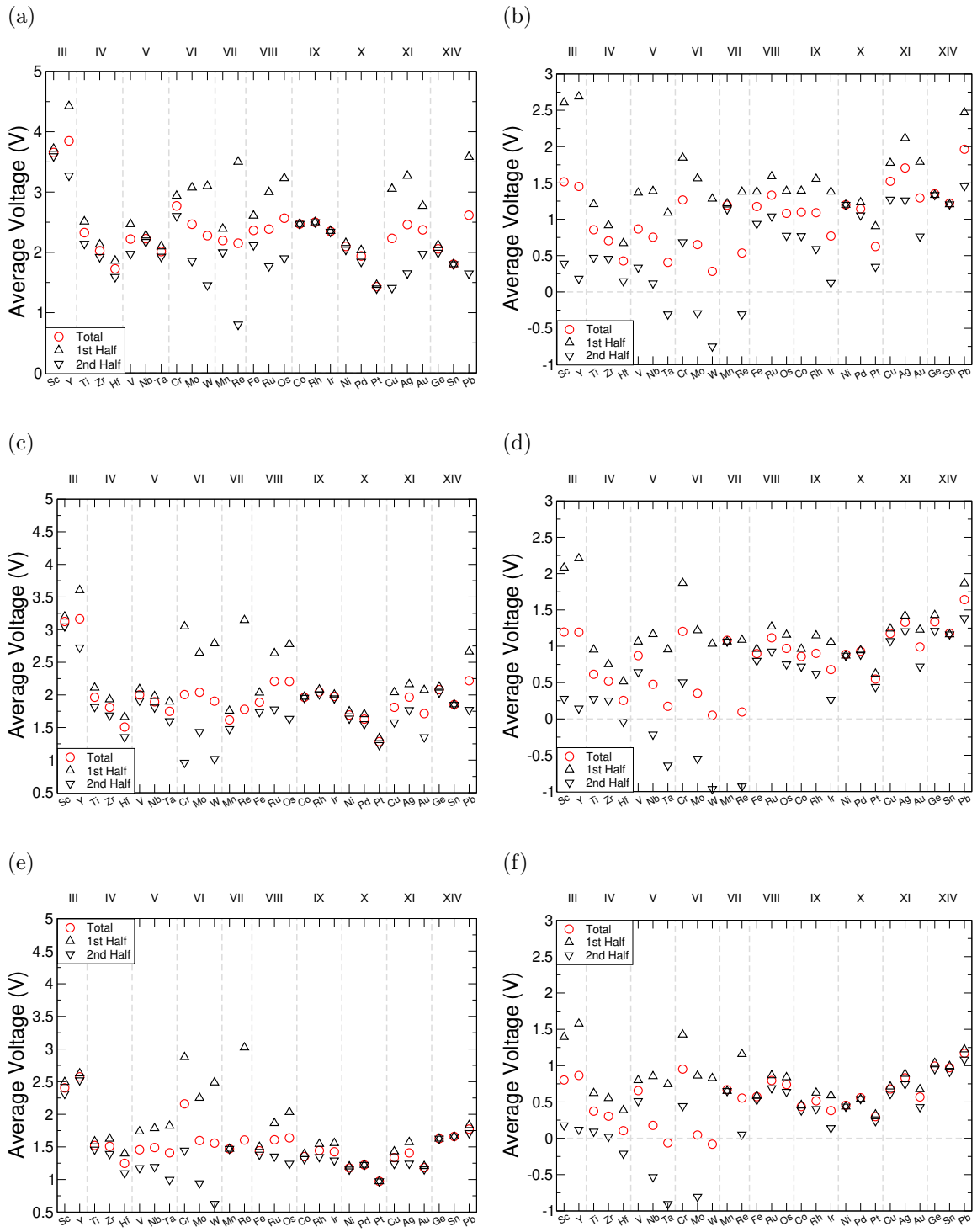

Figure S 22: Average intercalation voltages for each of the TMDCs intercalated with lithium and magnesium. The average lithium intercalation voltages are given in S22a, S22c, and S22e for the sulfides, selenide and tellurides, respectively. Equivalent data for the magnesium intercalation voltages are given in S22b, S22d, and S22f for the sulfides, selenide and tellurides, respectively.

	PBE Supercell Average Voltage (V)		PBE Primitive Cell Voltage (V)	
TMDC	Li	Mg	Li	Mg
ScS_2	3.655	1.515	3.655	1.515
YS_2	3.559	1.452	3.559	1.452
TiS_2	2.327	0.855	2.327	0.855
ZrS_2	2.027	0.703	2.027	0.703
HfS_2	1.726	0.426	1.726	0.426
VS_2	2.221	0.867	2.221	0.965
NbS_2	2.034	0.753	2.034	0.770
TaS_2	1.758	0.407	1.758	0.407
CrS_2	2.770	1.266	2.769	1.087
MoS_2	2.466	0.651	1.814	0.651
WS_2	1.584	0.283	1.584	0.283
MnS_2	2.196	1.194	2.196	1.276
ReS_2	2.152	0.535	1.688	0.556
FeS_2	2.364	1.176	2.354	1.187
RuS_2	2.385	1.332	2.385	1.332
OsS_2	2.210	1.082	2.210	1.099
CoS_2	2.471	1.097	2.471	1.097
RhS_2	2.499	1.090	2.500	1.090
IrS_2	2.348	0.769	2.348	0.769
NiS_2	2.100	1.199	2.100	1.216
PdS_2	1.941	1.143	1.941	1.160
PtS_2	1.430	0.625	1.430	0.641
CuS_2	2.231	1.523	2.232	1.539
AgS_2	2.178	1.706	2.178	1.707
AuS_2	1.825	1.293	1.825	1.294
GeS_2	2.057	1.351	2.057	1.351
SnS_2	1.803	1.222	1.804	1.222
PbS_2	2.616	1.963	2.618	1.981

Table S VI: Summary of average lithium and magnesium intercalation voltages for TMDC sulfides, using the PBE functional for the supercell and primitive cells. These have been calculated for the range $0 \leq a \leq 1$ in Li_aMS_2 and Mg_aMS_2.

	PBE Supercell Average Voltage (V)		PBE Primitive Cell Voltage (V)	
TMDC	Li	Mg	Li	Mg
$ScSe_2$	3.126	1.196	3.126	1.196
YSe_2	3.166	1.194	3.166	1.194
$TiSe_2$	1.964	0.614	1.962	0.631
$ZrSe_2$	1.808	0.519	1.809	0.519
$HfSe_2$	1.507	0.254	1.507	0.254
VSe_2	2.000	0.871	1.770	0.850
$NbSe_2$	1.626	0.476	1.630	0.493
$TaSe_2$	1.390	0.174	1.390	0.174
$CrSe_2$	2.005	1.205	2.593	1.205
$MoSe_2$	2.039	0.353	1.285	0.417
WSe_2	1.904	0.052	1.069	0.034
$MnSe_2$	1.617	1.082	1.901	1.082
$ReSe_2$	1.779	0.096	1.362	0.454
$FeSe_2$	1.886	0.899	1.881	0.899
$RuSe_2$	2.208	1.116	2.034	1.116
$OsSe_2$	2.205	0.971	1.936	0.971
$CoSe_2$	1.963	0.859	1.963	0.862
$RhSe_2$	2.046	0.903	2.046	0.903
$IrSe_2$	1.977	0.679	1.977	0.679
$NiSe_2$	1.693	0.888	1.693	0.889
$PdSe_2$	1.628	0.932	1.628	0.932
$PtSe_2$	1.284	0.548	1.284	0.559
$CuSe_2$	1.810	1.175	1.810	1.175
$AgSe_2$	1.830	1.331	1.754	1.331
$AuSe_2$	1.540	0.991	1.541	0.991
$GeSe_2$	2.081	1.338	2.081	1.338
$SnSe_2$	1.852	1.181	1.852	1.181
$PbSe_2$	2.218	1.642	2.218	1.643

Table S VII: Summary of average lithium and magnesium intercalation voltages for TMDC selenides, using the PBE functional for the supercell and primitive cells. These have been calculated for the range $0 \leq a \leq 1$ in Li_aMSe_2 and Mg_aMSe_2.

	PBE Supercell Average Voltage (V)		PBE Primitive Cell Voltage (V)	
TMDC	Li	Mg	Li	Mg
$ScTe_2$	2.404	0.802	2.404	0.802
YTe_2	2.573	0.865	2.573	0.865
$TiTe_2$	1.521	0.373	1.521	0.373
$ZrTe_2$	1.509	0.304	1.508	0.304
$HfTe_2$	1.247	0.104	1.247	0.104
VTe_2	1.546	0.656	1.257	0.673
$NbTe_2$	1.161	0.177	-0.685	0.177
$TaTe_2$	0.963	-0.063	0.963	-0.063
$CrTe_2$	2.160	0.952	2.297	0.952
$MoTe_2$	1.597	0.045	0.820	0.319
WTe_2	1.557	-0.082	0.610	0.098
$MnTe_2$	1.470	0.668	1.470	0.147
$ReTe_2$	1.605	0.554	1.284	0.571
$FeTe_2$	1.440	0.572	1.440	0.572
$RuTe_2$	1.609	0.795	1.609	0.795
$OsTe_2$	1.638	0.740	1.621	0.756
$CoTe_2$	1.352	0.438	1.351	0.444
$RhTe_2$	1.445	0.515	1.445	0.532
$IrTe_2$	1.425	0.381	1.425	0.381
$NiTe_2$	1.177	0.453	1.177	0.453
$PdTe_2$	1.224	0.558	1.224	0.558
$PtTe_2$	0.973	0.299	0.973	0.299
$AgTe_2$	1.408	0.678	1.408	0.678
$AuTe_2$	1.181	0.832	1.181	0.832
$CuTe_2$	1.336	0.569	1.335	0.569
$GeTe_2$	1.626	0.993	1.627	1.010
$SnTe_2$	1.659	0.972	1.659	0.972
$PbTe_2$	1.772	1.170	1.679	1.170

Table S VIII: Summary of average lithium and magnesium intercalation voltages for TMDC tellurides, using the PBE functional for the supercell and primitive cells. These have been calculated for the range $0 \leq a \leq 1$ in Li_aMTe_2 and Mg_aMTe_2.

MX_2	Range of a	Av. Voltage (V)	MX_2	Range of a	Av. Voltage (V)
YTe_2	$0 \leq a \leq \frac{7}{8}$	0.969	TaS_2	$0 \leq a \leq \frac{4}{8}$	1.083
$TiSe_2$	$0 \leq a \leq \frac{7}{8}$	0.702	$TaSe_2$	$0 \leq a \leq \frac{5}{8}$	0.740
$TiTe_2$	$0 \leq a \leq \frac{7}{8}$	0.408	MoS_2	$0 \leq a \leq \frac{5}{8}$	1.236
$ZrSe_2$	$0 \leq a \leq \frac{7}{8}$	0.575	$MoSe_2$	$0 \leq a \leq \frac{4}{8}$	1.215
$ZrTe_2$	$0 \leq a \leq \frac{7}{8}$	0.328	$MoTe_2$	$0 \leq a \leq \frac{4}{8}$	0.818
HfS_2	$0 \leq a \leq \frac{7}{8}$	0.468	WS_2	$0 \leq a \leq \frac{4}{8}$	1.196
$HfSe_2$	$0 \leq a \leq \frac{6}{8}$	0.408	WSe_2	$0 \leq a \leq \frac{4}{8}$	0.912
$HfTe_2$	$0 \leq a \leq \frac{6}{8}$	0.274	WTe_2	$0 \leq a \leq \frac{4}{8}$	0.711
VS_2	$0 \leq a \leq \frac{7}{8}$	0.971	ReS_2	$0 \leq a \leq \frac{4}{8}$	1.308
NbS_2	$0 \leq a \leq \frac{6}{8}$	1.052	$ReSe_2$	$0 \leq a \leq \frac{2}{8}$	2.292
$NbSe_2$	$0 \leq a \leq \frac{6}{8}$	0.819	$ReTe_2$	$0 \leq a \leq \frac{2}{8}$	2.193
$NbTe_2$	$0 \leq a \leq \frac{5}{8}$	0.692	PtS_2	$0 \leq a \leq \frac{6}{8}$	0.868

Table S IX: Table presenting, for TMDCs which have voltage profiles that go negative with magnesium intercalation, the range of concentrations a over which the voltage remains positive, and the average voltage calculated over this range.

Negative Voltages

In the main article, we highlight that some materials demonstrate voltages that become negative as the concentration of the intercalant species is increased. Though we have included these negative values in the calculation of the average voltages for easy comparison of materials, and so including these negative values within a calculation of the profile average is not necessarily appropriate. In Table SIX, we indicate the materials which have voltage profiles that become negative for some concentration of magnesium. We present the cutoff value of a and the average voltage calculated over this range. These values are of course slightly higher than those calculated with the negative values included. We find that many of the cutoff concentrations are either at $a = \frac{4}{8}$, corresponding to one donated electron per host metal atom, or close to fully intercalated at a concentration of $a = \frac{7}{8}$. The only material to show a negative voltage with lithium intercalation is $CrSe_2$ which has a cutoff concentration of $a = \frac{7}{8}$, with the average voltage up to the value being 2.292 V.

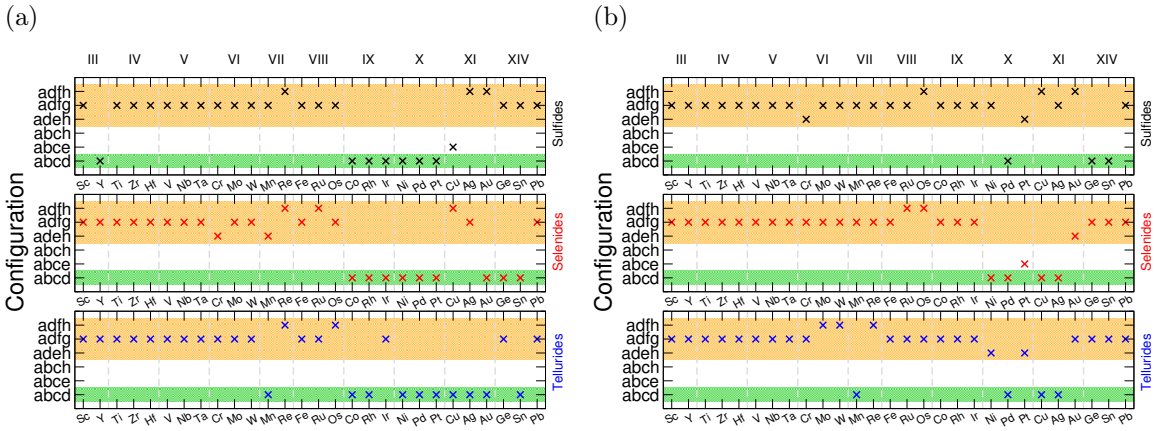

Figure S 23: Graphs indicating which intercalant configuration at $Li_{0.5}MX_2$ (S23a) and $Mg_{0.5}MX_2$ (S23b) is the lowest in energy. Indexing is used following Figure S1 and Table SII. The orange-shaded regions indicate intercalants spread evenly throughout the host structure, and the green-shaded regions indicate intercalants fill a single layer before intercalation of a second layer begins.

F. Clustering

We can comment on whether it is preferred for intercalants to intercalate a single vdW gap or to distribute across multiple layers. This is presented in Figure S23, where we focus on the $Li_{0.5}MX_2$ (S23a) and $Mg_{0.5}MX_2$ (S23b) intercalant concentration as an indicator, where we have used the indexing outlined in Figure S1 and Table SII. We indicate where intercalants spread evenly throughout the host structure with orange-shaded regions, and indicate where intercalants completely fill a single layer before occupying adjacent layers with the green-shaded regions. For lithium intercalation, most TMDCs have lithium spread evenly throughout the host[15], with the exception of Group IX and X TMDCs. There is then an even stronger preference for even-distribution of magnesium. This preference for intercalants to be distributed evenly throughout the host can be explained with a simple argument of minimising Coulombic repulsion between intercalant ions.

As mentioned in the main article and in the above discussion on how we obtain the intercalation voltage, it is possible for intercalants to separate into domains of different concentrations, beyond the configurations presented in Figure S23. For example, rather than have each cell of a crystal intercalated to $Li_{0.5}MX_2$, it may be preferred for domain/phase

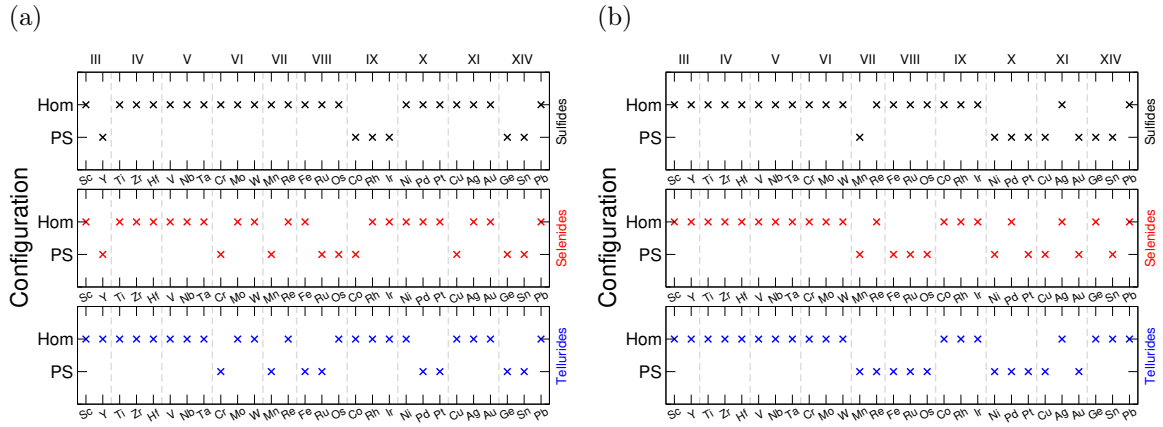

Figure S 24: Graphs depicting whether TMDCs are intercalated homogeneously (Hom) or whether there is domain/phase separation (PS). Results for lithium-intercalated TMDCs are presented in S24a, and those for magnesium-intercalated TMDCs are presented in S24b.

separation into Li_0MX_2 and Li_1MX_2, as has been demonstrated with $LiSnS_2$. We again consider the $Li_{0.5}MX_2$ and $Mg_{0.5}MX_2$ concentrations as an indicator for this separation, and present the results in Figure S24. Most materials show homogeneous (Hom) filling, and would follow the intercalant configuration presented in Figure S23. However, many materials show a phase separation (PS) into domains of different intercalant concentrations, for example (but not limited to) Li_0MX_2 and Li_1MX_2.

G. HSE06 Hybrid Functional

1. Energetics

Previous studies have shown that the choice of functional can lead to differences in predictions for properties important to electrode materials[16,17]. To account for the inaccurate calculation of exchange in GGA functionals such as PBE, and to evaluate the differences that can arise from choice of functional, the HSE06 hybrid functional[18–20] has been used for a selection of systems. Due to the higher computational cost of this functional compared to PBE, a smaller system was considered: the primitive unit cell of each of the 1T-TMDCs was used and intercalated with a single lithium atom. This corresponds to a lithium concentration equivalent to eight lithium atoms in the supercell system. Clearly, the primitive and supercell systems significantly differ in size, and so, to ensure that a comparison is made with an equivalently sized system, PBE calculations were also performed on the primitive cell with a single lithium intercalated per cell. For both the HSE and PBE calculations, geometric relaxations were converged to less than 0.01 eV/Å per atom, and electronic self-consistency is considered to an accuracy of 10^{-7} eV. Monkhorst-Pack k-point grids[2] of $6 \times 6 \times 6$ and $12 \times 12 \times 12$ were used for the HSE and PBE calculations, respectively.

The comparison of the PBE and HSE06 functionals are presented in Figures S25-S27 for selected lithium-intercalated TMDCs. In general, we identify an increase in both the voltage and E_{IS} using the HSE06 functional compared to PBE. The exceptions to this include SnS_2 (reduced by 0.14 V), ZrS_2 (reduced by 0.06 V), and HfS_2 (reduced by 0.04 V). The reduction in E_{IS} for these materials is shown to be due to lowering of the diagonal line described by equation (S12), corresponding to the boundary between the intercalated TMDC and the Li_2X crystal. Similarly, there is a raising of the horizontal line described by equation (S11), which describes the boundary between the intercalated and pristine TMDC structures. As such, the intercalated compound is reduced in favourability compared to both the pristine structure, and the conversion product Li_2X. By looking at the phase diagrams for the MoX_2 materials, Figure S26, we also not that as the chalcogen is varied down the group, the horizontal line is shifted further downwards.

In Table SX and Table SXI we present numerical values comparing HSE06 and PBE results.

TMDC	PBE Supercell Average Voltage (V)	PBE Primitive Cell Voltage (V)	HSE Primitive Cell Voltage (V)
ScS_2	3.655	3.655	4.231
YS_2	3.559	3.559	4.108
TiS_2	2.327	2.327	2.493
ZrS_2	2.027	2.027	1.966
HfS_2	1.726	1.726	1.684
MoS_2	2.466	1.814	2.066
IrS_2	2.348	2.348	2.922
$MoSe_2$	2.039	1.285	1.748
$MoTe_2$	1.597	0.820	1.849

Table S X: Summary of average TMDC lithium intercalation voltages, using the HSE06 functional for the primitive unit cells. PBE results using the supercell and primitive cell have been reproduced for easy comparison.

2. Geometric Structure

We also consider the difference in volumetric expansion. Using the PBE (HSE06) functional the expansion for SnS_2 is 9.81% (9.92%), for ZrS_2 it is 0.28% (-0.40%), and for HfS_2 it is 0.32% (-0.24%). Again, the differences between the two functionals are very small.

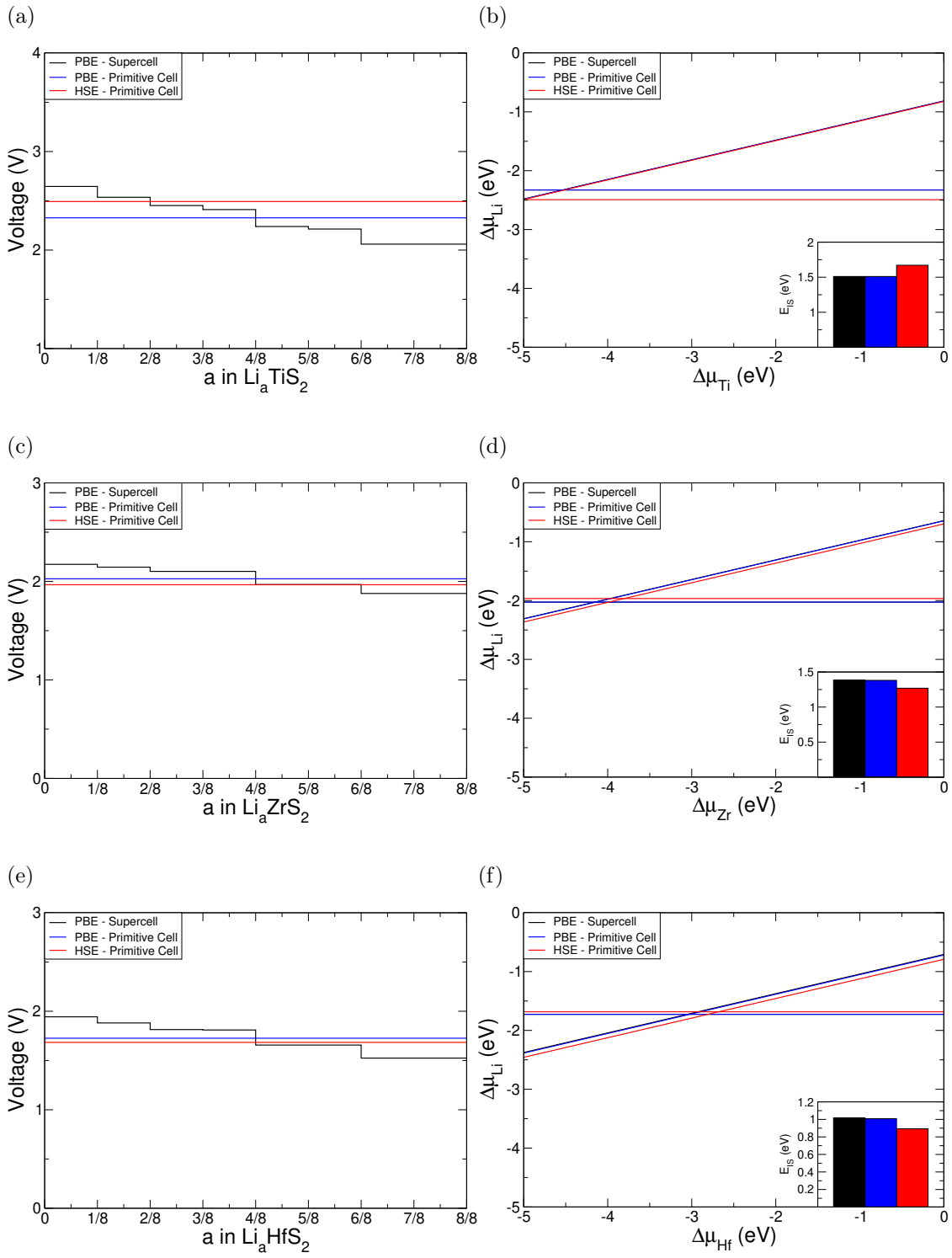

Figure S 25: Comparison of results using the PBE and HSE06 functionals. S25a, S25c, and S25e present the voltages for TiS_2, ZrS_2, and HfS_2, respectively. S25b, S25d, and S25f present the phase diagrams for TiS_2, ZrS_2, and HfS_2, respectively. The insets show the values of E_{IS}.

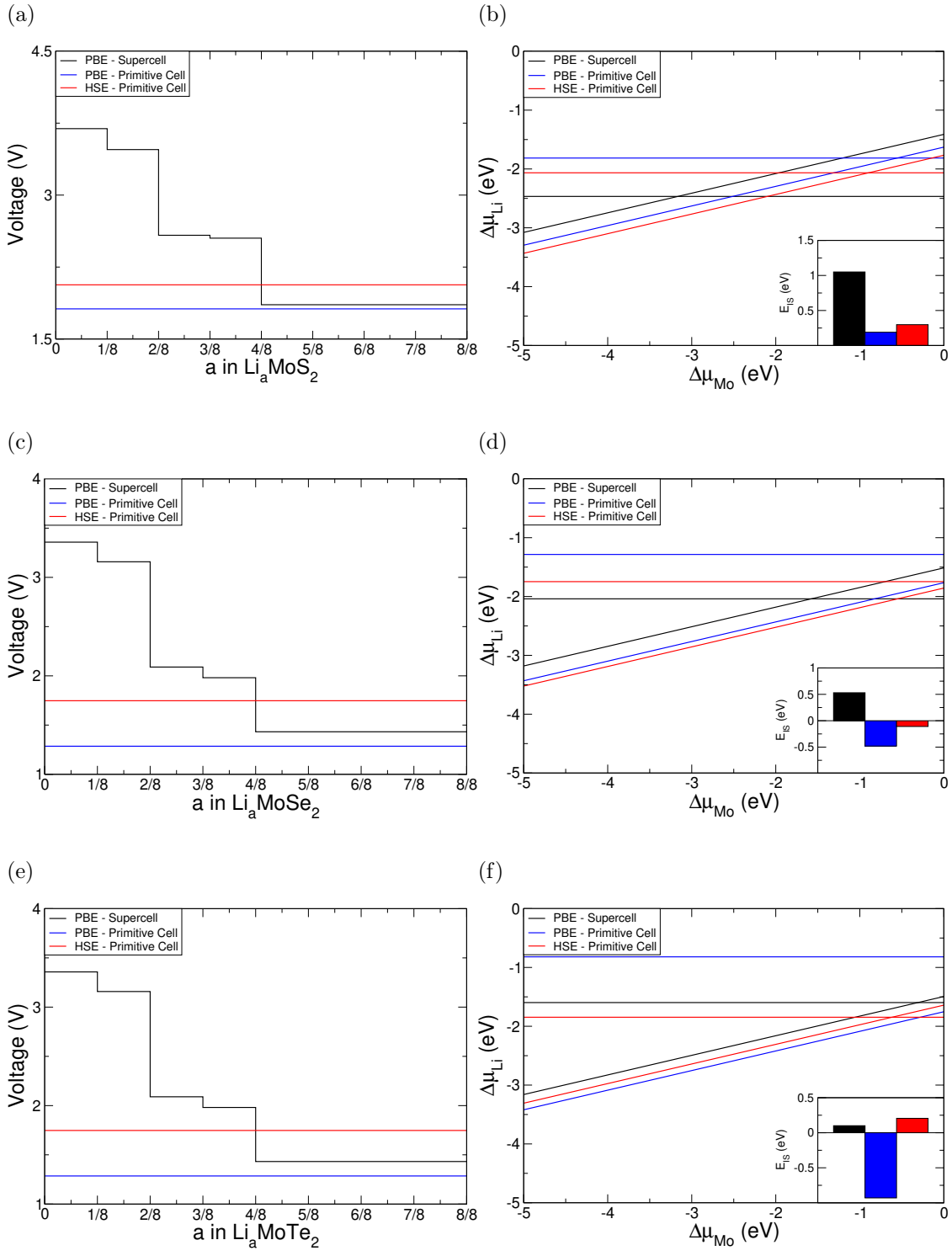

Figure S 26: Comparison of results using the PBE and HSE06 functionals. S26a, S26c, and S26e present the voltages for MoS_2, $MoSe_2$, and $MoTe_2$, respectively. S26b, S26d, and S26f present the phase diagrams for MoS_2, $MoSe_2$, and $MoTe_2$, respectively. The insets show the values of E_{IS}.

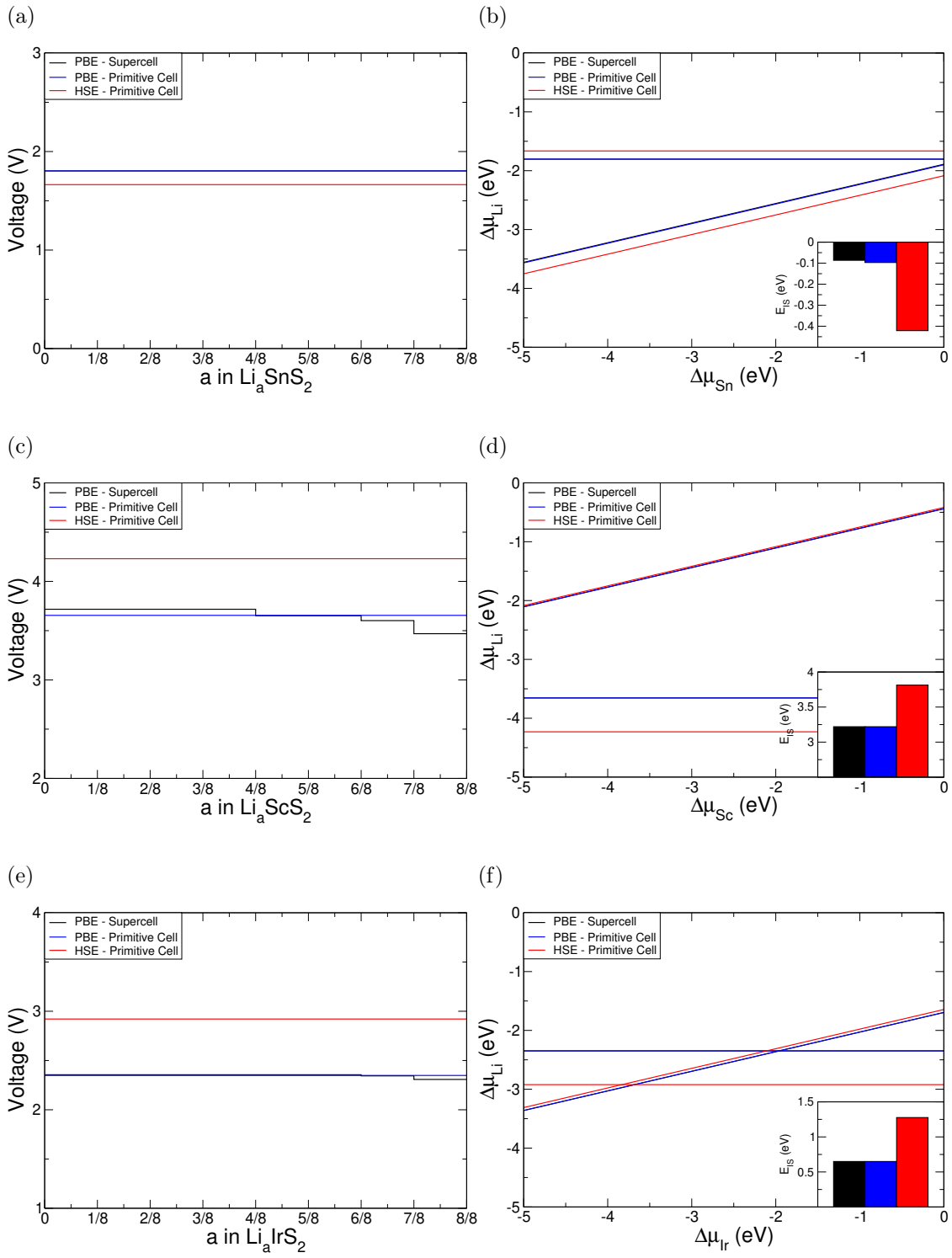

Figure S 27: Comparison of results using the PBE and HSE06 functionals. S27a, S27c, and S27e present the voltages for SnS_2, ScS_2, and IrS_2, respectively. S27b, S27d, and S27f present the phase diagrams for SnS_2, ScS_2, and IrS_2, respectively. The insets show the values of E_{IS}.

TMDC	PBE Supercell E_{IS} (eV)	PBE Primitive Cell E_{IS} (eV)	HSE Primitive Cell E_{IS} (eV)
ScS_2	3.22	3.22	3.81
YS_2	3.58	3.20	3.78
TiS_2	1.51	1.51	1.67
ZrS_2	1.38	1.38	1.27
HfS_2	1.02	1.02	0.89
MoS_2	1.05	0.19	0.30
IrS_2	0.65	0.65	1.28
SnS_2	-0.09	-0.09	-0.42
$MoSe_2$	0.53	-0.48	-0.11
$MoTe_2$	0.10	-0.93	0.21

Table S XI: Summary of average E_{IS} values for lithium intercalation of TMDCs, using the HSE06 functional for the primitive unit cells. PBE results using the supercell and primitive cell have been reproduced for easy comparison.

H. $\mathbf{E}_{IS}$

In the main article, we presented values for the metric of stability, E_{IS}, for each of the sulfide TMDCs. Here, we present the equivalent data for the selenide and telluride materials.

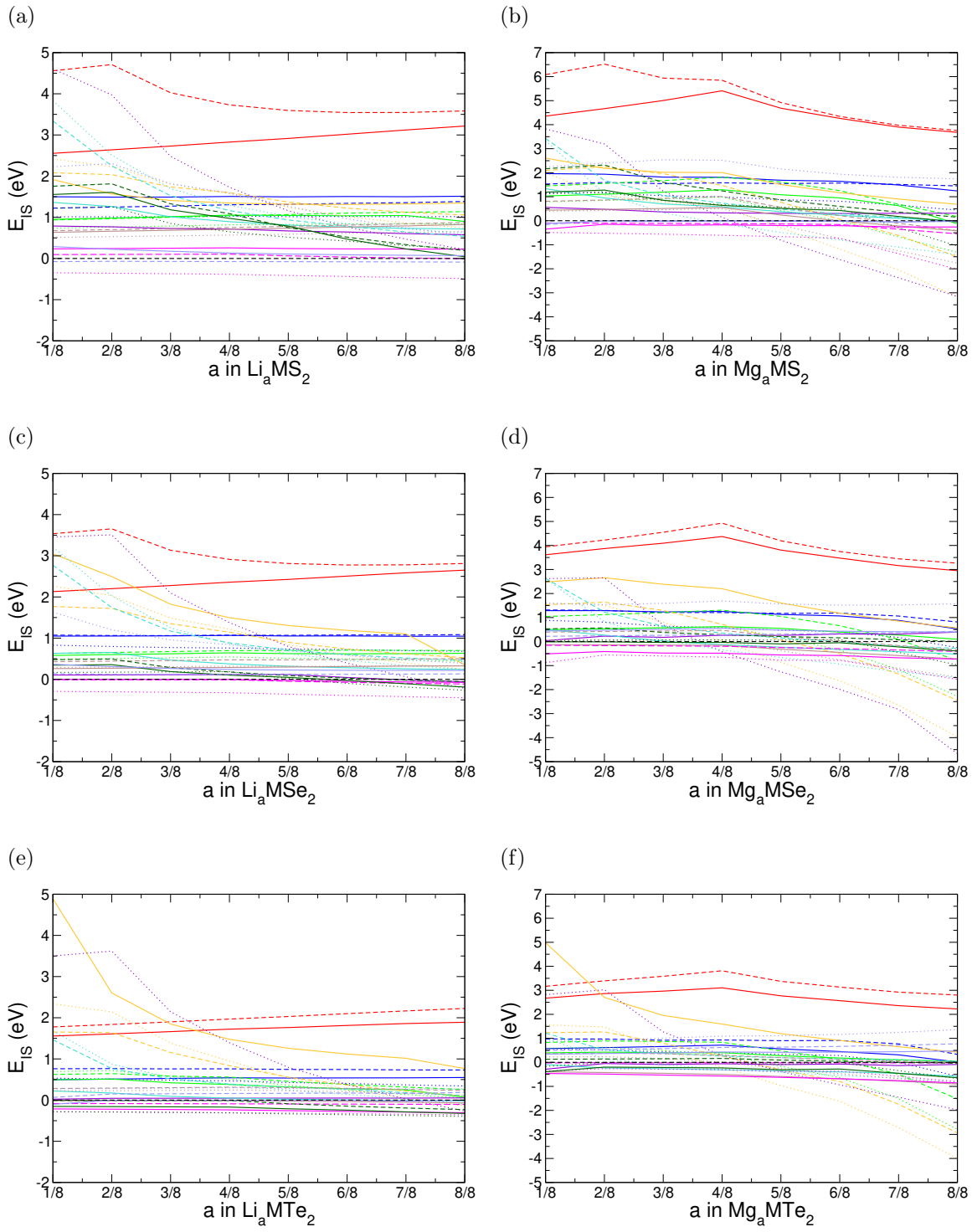

Figure S 28: Variation in E_{IS} with lithium (S28a, S28c, and S28e) and magnesium (S28b, S28d, and S28f) intercalation for each of the TMDCs. Full legend is given in Figure S18.

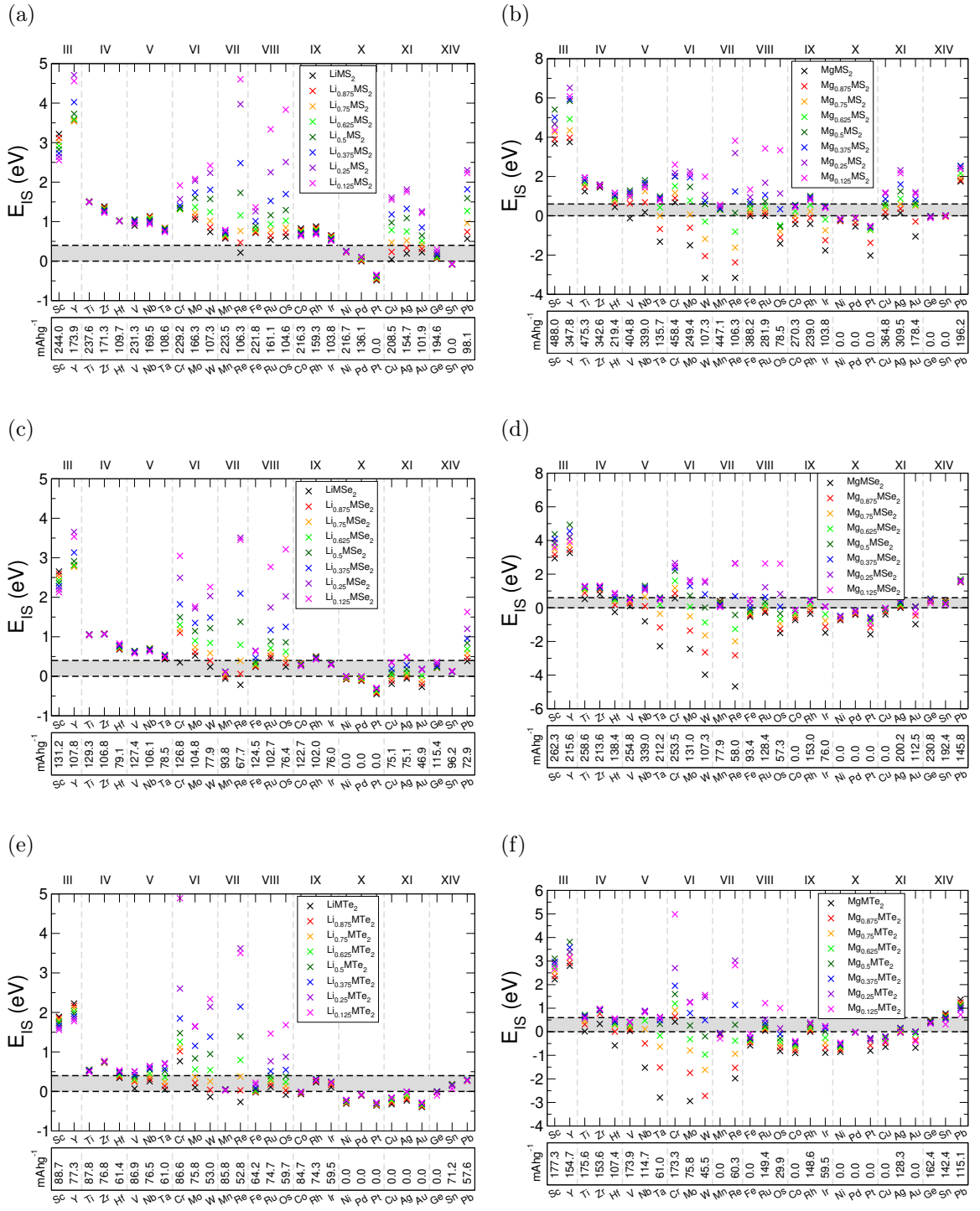

Figure S 29: Average E_{IS} values for each of the TMDCs intercalated with lithium and magnesium. S29a, S29c, and S29e present the values of E_{IS} for the sulfides, selenides and tellurides intercalated with lithium, respectively. S29b, S29d, and S29f present the values of E_{IS} for the sulfides, selenides and tellurides intercalated with magnesium, respectively. The reversible intercalation capacity, determined from the range over which E_{IS} remains positive, is given at the bottom of each figure in mAhg^{-1}.

	PBE Supercell E_{IS} (eV)		PBE Primitive Cell E_{IS} (eV)	
TMDC	Li	Mg	Li	Mg
ScS_2	3.22	3.68	3.22	3.68
YS_2	3.58	3.76	3.20	3.76
TiS_2	1.51	1.24	1.51	1.24
ZrS_2	1.38	1.45	1.38	1.45
HfS_2	1.02	0.44	1.02	0.44
VS_2	0.90	-0.13	0.90	0.27
NbS_2	1.14	0.17	0.88	0.17
TaS_2	0.84	-1.32	0.50	-1.32
CrS_2	1.35	0.68	1.35	-0.10
MoS_2	1.05	-1.50	0.19	-1.50
WS_2	0.74	-3.17	-0.19	-3.17
MnS_2	0.58	0.31	0.58	0.64
ReS_2	0.22	-3.16	-0.40	-3.14
FeS_2	0.72	-0.01	0.70	0.03
RuS_2	0.54	-0.01	0.54	-0.01
OsS_2	0.62	-1.41	0.15	-1.41
CoS_2	0.83	-0.42	0.83	-0.42
RhS_2	0.88	-0.41	0.88	-0.41
IrS_2	0.65	-1.76	0.65	-1.76
NiS_2	0.23	-0.26	0.23	-0.26
PdS_2	0.00	-0.55	-0.00	-0.55
PtS_2	-0.49	-2.02	-0.49	-2.02
CuS_2	0.04	-0.05	0.04	-0.05
AgS_2	0.19	0.15	-0.18	0.15
AuS_2	0.23	-1.05	-0.51	-1.05
GeS_2	0.07	-0.02	0.07	-0.02
SnS_2	-0.09	0.01	-0.09	0.01
PbS_2	0.57	1.75	0.57	1.75

Table S XII: Summary of lithium and magnesium E_{IS} values for TMDC sulfides. These have been calculated for the Li_aMS_2 and Mg_aMS_2 compositions, using the PBE functional for the supercell and primitive cells.

	PBE Supercell E_{IS} (eV)		PBE Primitive Cell E_{IS} (eV)	
TMDC	Li	Mg	Li	Mg
$ScSe_2$	2.65	2.95	2.65	2.95
YSe_2	2.81	3.26	2.81	3.26
$TiSe_2$	1.05	0.52	1.05	0.53
$ZrSe_2$	1.09	0.82	1.09	0.82
$HfSe_2$	0.68	-0.25	0.68	-0.25
VSe_2	0.63	0.09	0.32	0.01
$NbSe_2$	0.70	-0.80	0.34	-0.80
$TaSe_2$	0.43	-2.28	-0.04	-2.28
$CrSe_2$	0.35	0.57	1.13	0.57
$MoSe_2$	0.53	-2.45	-0.48	-2.20
WSe_2	0.24	-3.97	-0.87	-4.04
$MnSe_2$	-0.06	0.39	0.32	0.39
$ReSe_2$	-0.22	-4.67	-0.77	-3.24
$FeSe_2$	0.24	-0.52	0.23	-0.52
$RuSe_2$	0.46	-0.28	0.22	-0.28
$OsSe_2$	0.24	-1.50	-0.12	-1.50
$CoSe_2$	0.33	-0.73	0.33	-0.71
$RhSe_2$	0.50	-0.35	0.50	-0.35
$IrSe_2$	0.33	-1.48	0.33	-1.48
$NiSe_2$	-0.08	-0.73	-0.07	-0.73
$PdSe_2$	-0.11	-0.41	-0.11	-0.41
$PtSe_2$	-0.45	-1.58	-0.45	-1.53
$CuSe_2$	-0.19	-0.39	-0.19	-0.39
$AgSe_2$	-0.06	0.00	-0.34	0.00
$AuSe_2$	-0.27	-0.97	-0.50	-0.97
$GeSe_2$	0.22	0.39	0.22	0.39
$SnSe_2$	0.13	0.42	0.13	0.42
$PbSe_2$	0.39	1.57	0.39	1.58

Table S XIII: Summary of lithium and magnesium E_{IS} values for TMDC selenides. These have been calculated for the Li_aMSe_2 and Mg_aMSe_2 compositions, using the PBE functional for the supercell and primitive cells.

	PBE Supercell E_{IS} (eV)		PBE Primitive Cell E_{IS} (eV)	
TMDC	Li	Mg	Li	Mg
$ScTe_2$	1.89	2.22	1.89	2.22
YTe_2	2.23	2.80	2.23	2.80
$TiTe_2$	0.55	0.01	0.55	0.01
$ZrTe_2$	0.73	0.33	0.73	0.33
$HfTe_2$	0.34	-0.58	0.34	-0.58
VTe_2	0.07	0.04	-0.20	0.04
$NbTe_2$	0.26	-1.52	-0.18	-1.52
$TaTe_2$	0.05	-2.79	-0.55	-2.79
$CrTe_2$	0.77	0.43	0.95	0.43
$MoTe_2$	0.10	-2.94	-0.93	-1.84
WTe_2	-0.13	-4.00	-1.40	-3.28
$MnTe_2$	0.05	-0.09	0.05	-2.17
$ReTe_2$	-0.27	-1.98	-0.69	-1.98
$FeTe_2$	-0.02	-0.58	-0.02	-0.58
$RuTe_2$	0.11	0.04	0.11	0.04
$OsTe_2$	-0.08	-0.82	-0.11	-0.82
$CoTe_2$	-0.07	-0.90	-0.07	-0.88
$RhTe_2$	0.23	0.00	0.23	0.00
$IrTe_2$	0.11	-0.89	0.11	-0.89
$NiTe_2$	-0.31	-0.86	-0.31	-0.86
$PdTe_2$	-0.11	-0.02	-0.11	-0.02
$PtTe_2$	-0.36	-0.80	-0.36	-0.80
$CuTe_2$	-0.32	-0.64	-0.32	-0.64
$AgTe_2$	-0.23	-0.04	-0.23	-0.04
$AuTe_2$	-0.40	-0.68	-0.40	-0.68
$GeTe_2$	-0.01	0.47	-0.01	0.47
$SnTe_2$	0.19	0.77	0.19	0.77
$PbTe_2$	0.27	1.36	0.15	1.36

Table S XIV: Summary of lithium and magnesium E_{IS} values for TMDC telluride. These have been calculated for the Li_aMTe_2 and Mg_aMTe_2 compositions, using the PBE functional for the supercell and primitive cells.

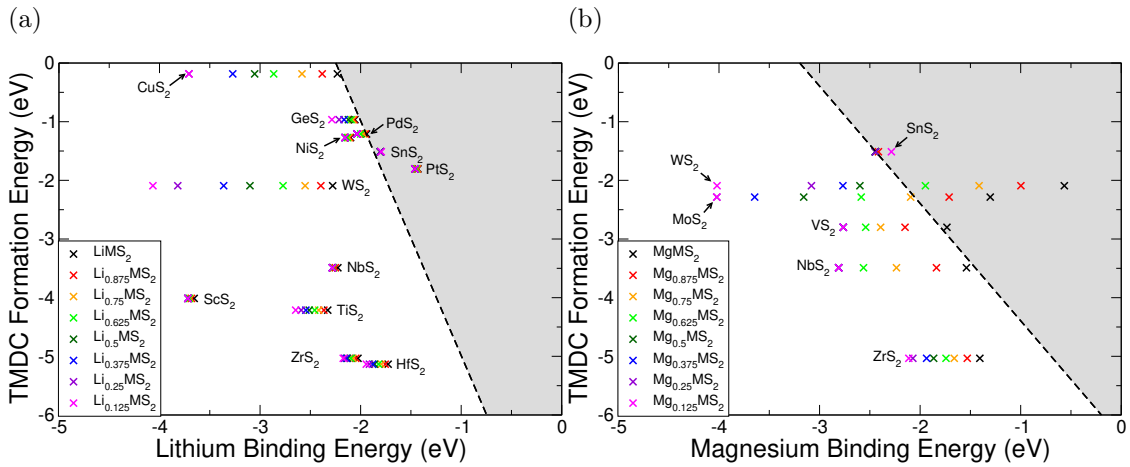

Figure S 30: Comparison of TMDC formation energy (equation (S20)) and intercalant binding energy (equation (S21)) for different intercalant concentrations of selected TMDCs. S30a and S30b present results for lithium and magnesium intercalation, respectively. The shaded region indicates where conversion is energetically favourable, equivalent to negative values of E_{IS}.

I. Formation Energy vs. Intercalant Binding Energy

Two quantities that are more commonly used for first-principles material evaluation are formation energy and binding energy. The TMDC binding energy is given by,

$$\Delta H(\mathrm{MX_2}) = E(\mathrm{MX_2}) - [E(\mathrm{M}) + 2E(\mathrm{X})]. \tag{S20}$$

The formation energy describes the energy required to form a material from the constituent elements, and so gives an indication of the strength of the M-X bond. The more negative a value of $\Delta H(\mathrm{MX_2})$ the stronger the M-X bond, and hence the more resistant the TMDC is to conversion. Similarly, the intercalant binding energy is given by,

$$E_b = E(\mathrm{Li_aMX_2}) - [E(\mathrm{MX_2}) + aE(\mathrm{Li})] \tag{S21}$$

(or equivalent for magnesium). This then gives the energy required to add some quantity a of an intercalant to the host TMDC, again with negative values signifying a more favourable intercalation reaction, hence indicating the strength of the interaction between intercalant

and TMDC. To resist the conversion reaction, a TMDC should possess a large (negative) formation energy, large (negative) intercalant binding energy, or ideally both.

In terms of the above two quantities, we can determine the limits of stability, which are,

$$\begin{aligned} \Delta H(\mathrm{MX_2}) + 4\mathrm{E_b} &\leq 2\Delta H(\mathrm{Li_2X}) \\ \Delta H(\mathrm{MX_2}) + 2\mathrm{E_b} &\leq 2\Delta H(\mathrm{MgX}). \end{aligned} \tag{S22}$$

which requires the formation energy of the TMDC and the intercalant binding energy to be lower that the formation energy of the appropriate conversion product ($\Delta H(\mathrm{Li_2X})$ or $\Delta H(\mathrm{MgX})$). In Figure S30a we plot the TMDC formation energy against the lithium binding energy, and also indicate the boundary described by equation (S22). Here, it is now easy to see that materials that possess a negative value of E_{IS} and are unstable against intercalation (such as $\mathrm{PdS_2}$, $\mathrm{SnS_2}$, or $\mathrm{CuTe_2}$) are those with low TMDC formation energy and low lithium binding energy.

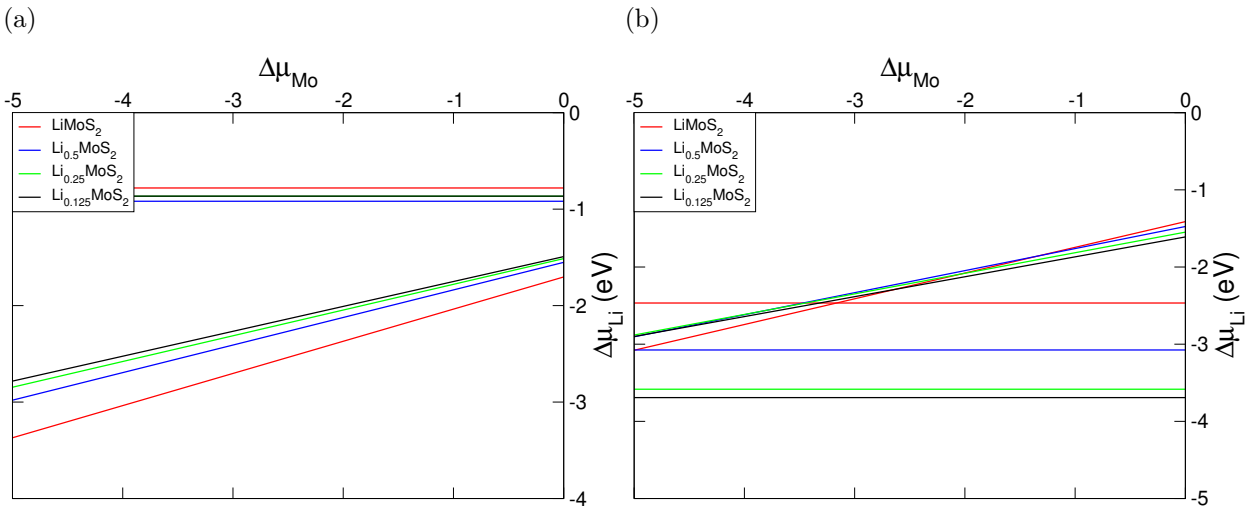

Figure S 31: Figure S31a shows the phase diagram for intercalated 2H-MoS_2 and Figure S31b shows the phase diagram for intercalated 1T-MoS_2, for varying lithium concentrations.

J. MoS_2 H→T Transition

We can further demonstrate the usefulness of these phase diagrams by considering the intercalated 2Hc- and 1T-MoS_2 structures, shown in Figure S31a and Figure S31b, respectively. It has been widely reported that, upon intercalation with lithium, 2H-MoS_2 undergoes a phase transition to 1T-MoS_2. Within the phase diagrams, this presents itself as the 2H-MoS_2 having no window of stability for the intercalated structure, with a negative value of E_{IS}. The 1T-MoS_2 phase, however, has a value of $E_{IS} = 1.055$ eV. As such, the intercalated layered structure must convert to the T-phase, otherwise the decomposition into Li_2S becomes energetically favourable.

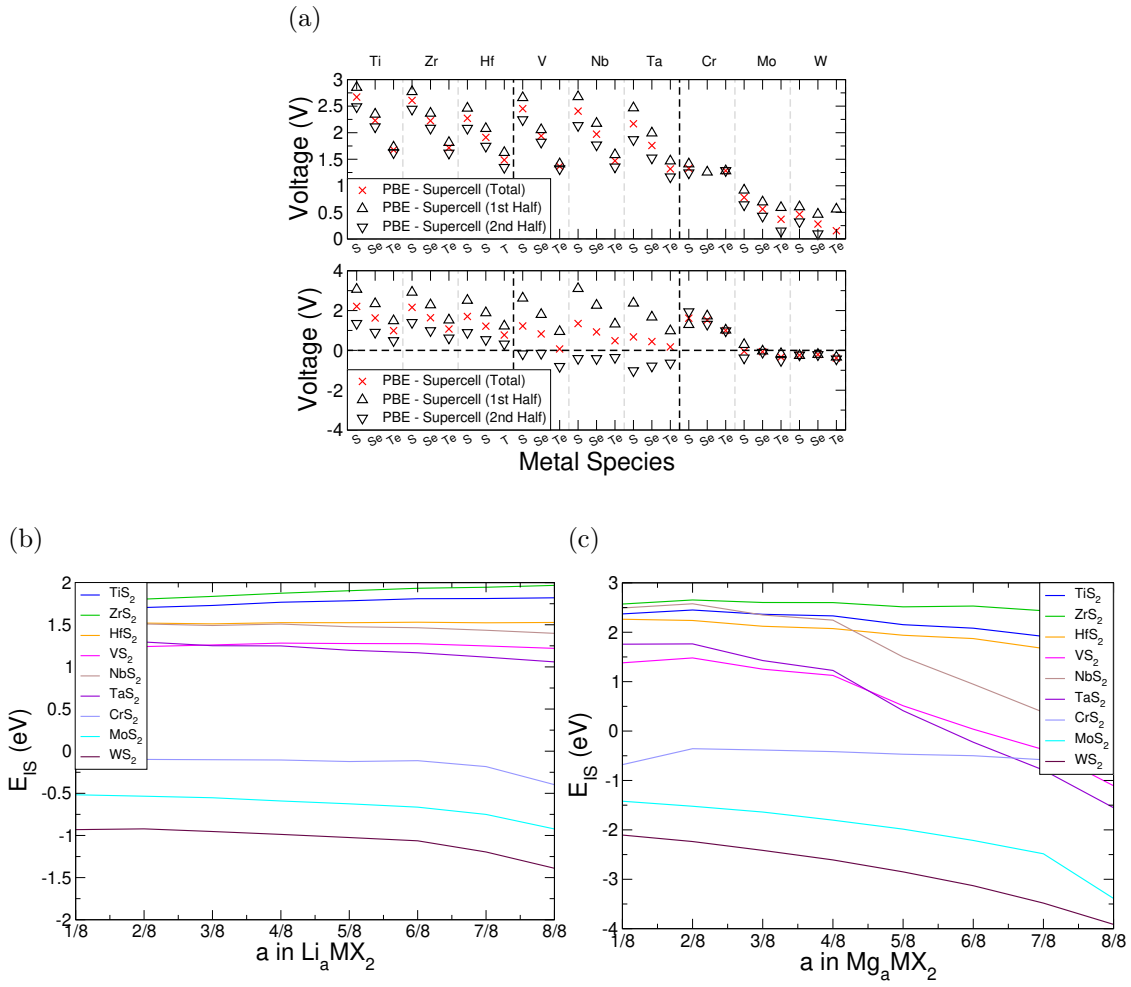

Figure S 32: H-phase intercalation voltages (S32a) and values of E_{IS} for lithium (S32b) and magnesium (S32c) intercalation into H-phase TMDCs.

K. H-Phase Data

We present here the point of phase crossover, the average intercalation voltage, and the final value of E_{IS} in the $LiMX_2$ and $MgMX_2$ compounds in Table SXV (sulfides), Table SXVI (selenides), and Table SXVII (tellurides). The crossover indicates the value of a in Li_aMX_2 at which the T- and Hc-phases are equal in energy, determined by using linear fits between the MX_2 and $LiMX_2$ compounds. For the Group IV TMDCs, the transition is from T-phase to Hc-phase, for Group V TMDCs the crossover indicates the T-Hc phase transition, with negative values indicating that the T phase is never favourable, and for the Group VI TMDCs the transition is from Hc-phase to T-phase for increasing a. For magnesium to Mg_aMX_2, this single linear fit is not sufficient as there are two behaviours arising from the

	Crossover		Average Voltage (V)		E_{IS} (eV)	
TMDC	Li	Mg	Li	Mg	Li	Mg
TiS_2	1.311	0.877	2.671	1.088	1.820	1.785
ZrS_2	0.991	0.608	2.608	1.063	1.967	2.384
HfS_2	1.196	0.648	2.272	0.835	1.527	1.495
VS_2	-0.164	0.268	2.452	0.596	1.220	-1.107
NbS_2	-0.378	0.817	2.406	0.657	1.399	-0.140
TaS_2	-0.282	0.782	2.168	0.321	1.059	-1.552
CrS_2	0.372	0.258	1.327	0.792	-0.397	-0.675
MoS_2	0.481	0.283	0.780	-0.039	-0.923	-3.388
WS_2	0.483	0.945	0.462	-0.138	-1.389	-3.913

Table S XV: Data for intercalated H-phase TMDC sulfides, including the intercalant concentration for phase crossover (a in Li_aMS_2 or Mg_aMS_2), average intercalation voltage, and E_{IS} values at $a = 1$.

	Crossover		Average Voltage (V)		E_{IS} (eV)	
TMDC	Li	Mg	Li	Mg	Li	Mg
$TiSe_2$	1.435	1.052	2.229	0.797	1.274	0.872
$ZrSe_2$	1.104	0.690	2.225	0.802	1.488	1.555
$HfSe_2$	1.337	0.719	1.912	0.590	1.040	0.617
VSe_2	0.482	0.082	1.939	0.396	0.560	-1.708
$NbSe_2$	-0.628	0.474	1.972	0.446	0.817	-0.871
$TaSe_2$	-3.305	0.716	1.759	0.205		
$CrSe_2$	0.035	0.293	-10.184	0.743	-15.759	-0.786
$MoSe_2$	0.459	0.270	0.561	-0.049	-1.219	-3.318
WSe_2	0.463	0.738	0.279	-0.121	-1.675	-3.844

Table S XVI: Data for intercalated H-phase TMDC selenides, including the intercalant concentration for phase crossover (a in Li_aMSe_2 or Mg_aMSe_2), average intercalation voltage, and E_{IS} values at $a = 1$.

double valency of the magnesium intercalant. We instead extrapolate a linear fit between the unintercalated MX_2 and $Mg_{0.5}MX_2$ compounds, with the charge transferred in $Mg_{0.5}MX_2$ corresponding to the full charge transfer of $LiMX_2$ due to the double valency of magnesium, and a second fit between the $Mg_{0.5}MX_2$ and $MgMX_2$ points. We identify that the Group IV

	Crossover		Average Voltage (V)		E_{IS} (eV)	
TMDC	Li	Mg	Li	Mg	Li	Mg
$TiTe_2$	2.208	1.364	1.676	0.477	0.641	0.156
$ZrTe_2$	1.701	0.791	1.715	0.520	0.890	0.913
$HfTe_2$	1.770	0.803	1.486	0.369	0.521	0.119
VTe_2	-0.033	-0.004	1.367	0.018	-0.051	-2.520
$NbTe_2$	1.178	0.775	1.470	0.225	0.238	-1.239
$TaTe_2$	0.080	0.731	1.318	0.069		-2.187
$CrTe_2$	0.337	0.158	1.284	0.483	-0.304	-1.088
$MoTe_2$	0.416	0.923	0.369	-0.186	-1.364	-3.285
WTe_2	0.403	0.783	0.153	-0.209	-1.818	-3.875

Table S XVII: Data for intercalated H-phase TMDC tellurides, including the intercalant concentration for phase crossover (a in Li_aMTe_2 or Mg_aMTe_2), average intercalation voltage, and E_{IS} values at $a = 1$.

TMDCs undergo T- to H-phase transitions, whereas the Group V and VI TMDCs undergo H- to T-transitions. $MgVTe_2$ does not transition (indicated by the negative crossover value), remaining in the T-phase throughout.

We do note some slight changes to the intercalation voltages, with the H-phase voltages being higher than the T-phase for Group IV TMDCs, and lower in the H-phase than the T-phase for the Group VI TMDCs. There is a mix for the Group V TMDCs. We present in Figure S32 the evolution of E_{IS} with lithium (Figure S32b) and magnesium (Figure S32c) intercalant concentration in H-phase TMDC sulfides. The values of E_{IS} at full intercalation are also given in Table SXV, Table SXVI, and Table SXVII. In general, we see the same trends as are observed in the T-phase: with increased lithium intercalation, the Group IV and V TMDCs retain a relatively constant value of E_{IS}, and the Group VI TMDCs show a drop in stability for higher concentrations. With magnesium intercalation, we again notice the drop in stability for intercalation concentration greater than $a = 0.5$ attributed to the double valency of magnesium. The Group IV materials remain stable across the range of concentrations, as do the Group V materials for concentrations lower than $a = 0.5$. Beyond this intercalant concentration they become unstable. The MoX_2 and WX_2 materials show no positive values of E_{IS}. For each of the TMDCs considered here, the heavier chalcogens show reduced stability and hence a higher susceptibility to conversion reactions.

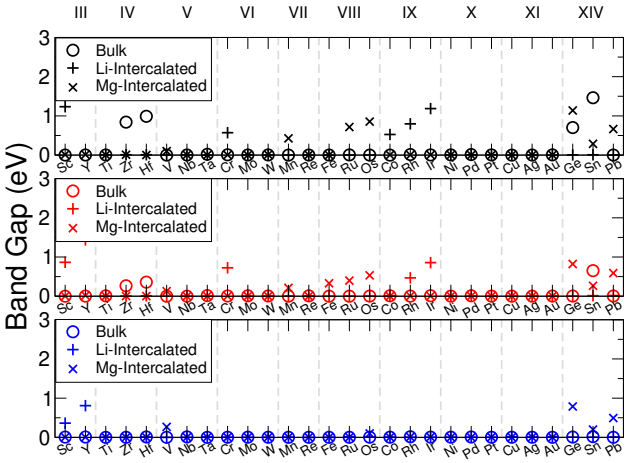

Figure S 33: Electronic band gap sizes for pristine bulk (circles), lithium-intercalated (pluses), and magnesium-intercalated (crosses) TMDCs. Sulfide data is in black (top), selenide data is in red (middle), and telluride data is in blue (bottom).

L. Electronic Structure

We present in Figure S33 the electronic band gaps for each of the pristine, lithium-intercalated, and magnesium-intercalated materials. It is clear to see that the vast majority possess no band gap, and so should be electronically conductive. This agrees with previous works which have established the increased conductivity of T-phase TMDCs over their H-phase counterparts. The numerical values of the band gap are presented in Table SXVIII.

In the main article, we commented on the nature of the valence and conduction bands in terms of their orbital character. In Figure S34 we present the orbital-projected density of states for the selection of materials that were highlighted in the main article, i.e. NbS_2, HfS_2, and GeS_2.

	Sulfide Band Gap (eV)			Selenide Band Gap (eV)			Telluride Band Gap (eV)		
M	Bulk	Li	Mg	Bulk	Li	Mg	Bulk	Li	Mg
Sc	0.002	1.234	0.009	0.000	0.865	0.001	0.007	0.362	0.003
Y	0.003	1.847	0.011	0.003	1.438	0.019	0.008	0.809	0.004
Ti	0.003	0.003	0.004	0.009	0.002	0.001	0.001	0.005	0.002
Zr	0.841	0.009	0.009	0.266	0.005	0.005	0.001	0.001	0.002
Hf	0.989	0.008	0.002	0.359	0.009	0.002	0.011	0.011	0.001
V	0.000	0.001	0.101	0.001	0.002	0.129	0.001	0.001	0.267
Nb	0.003	0.005	0.004	0.001	0.002	0.001	0.012	0.001	0.003
Ta	0.020	0.000	0.001	0.015	0.001	0.002	0.000	0.011	0.004
Cr	0.007	0.571	0.004	0.007	0.725	0.004	0.003	0.004	0.001
Mo	0.002	0.008	0.002	0.011	0.003	0.001	0.005	0.003	0.002
W	0.004	0.003	0.011	0.006	0.005	0.001	0.002	0.004	0.002
Mn	0.000	0.002	0.427	0.002	0.005	0.213	0.001	0.006	0.003
Re	0.001	0.001	0.005	0.009	0.008	0.001	0.002	0.000	0.001
Fe	0.001	0.000	0.000	0.001	0.000	0.331	0.001	0.003	0.000
Ru	0.004	0.003	0.715	0.001	0.003	0.398	0.002	0.011	0.002
Os	0.000	0.001	0.855	0.004	0.003	0.533	0.004	0.008	0.099
Co	0.000	0.526	0.002	0.011	0.011	0.001	0.005	0.009	0.003
Rh	0.014	0.797	0.001	0.003	0.468	0.005	0.014	0.004	0.009
Ir	0.004	1.185	0.004	0.013	0.857	0.003	0.006	0.004	0.008
Ni	0.005	0.001	0.004	0.002	0.004	0.002	0.004	0.006	0.001
Pd	0.012	0.005	0.000	0.011	0.004	0.004	0.008	0.006	0.000
Pt	0.005	0.008	0.002	0.003	0.007	0.004	0.003	0.005	0.005
Cu	0.000	0.003	0.001	0.003	0.002	0.001	0.003	0.013	0.002
Ag	0.002	0.003	0.000	0.002	0.005	0.002	0.004	0.010	0.004
Au	0.006	0.002	0.005	0.005	0.004	0.001	0.001	0.018	0.001
Ge	0.702	0.004	1.138	0.005	0.002	0.822	0.007	0.005	0.787
Sn	1.463	0.007	0.287	0.653	0.014	0.267	0.017	0.005	0.199
Pb	0.001	0.003	0.664	0.004	0.018	0.591	0.002	0.009	0.493

Table S XVIII: Electronic band gaps, obtained from the difference in energy between the highest occupied state and lowest unoccupied state.

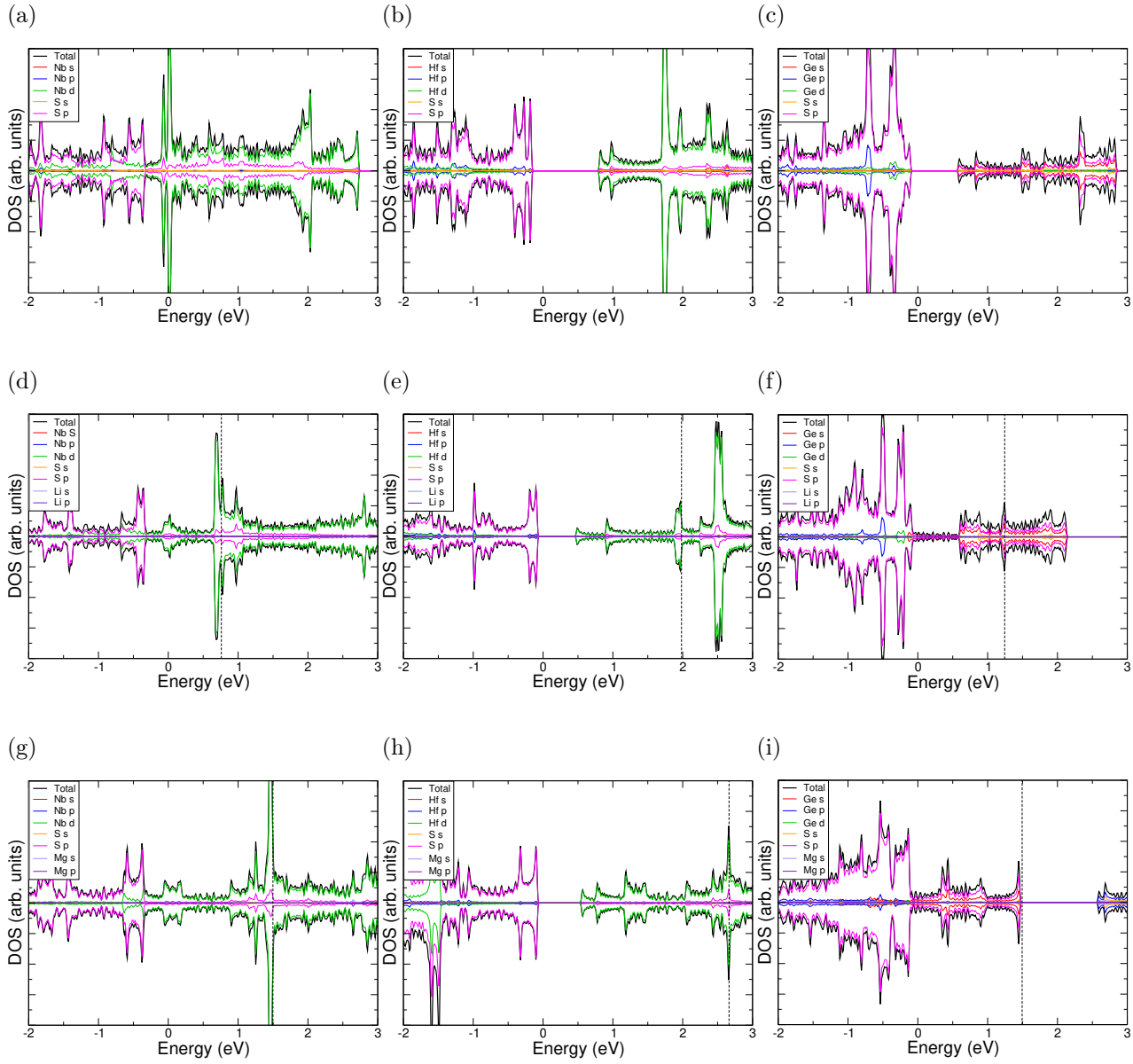

Figure S 34: Atomic-orbital decomposed density of states for selected materials, NbS_2 (S34a, S34d, and S34g), HfS_2 (S34b, S34e, and S34h), and GeS_2 (S34c, S34f, and S34i). These have been aligned as the electronic structures presented in the main article have been.

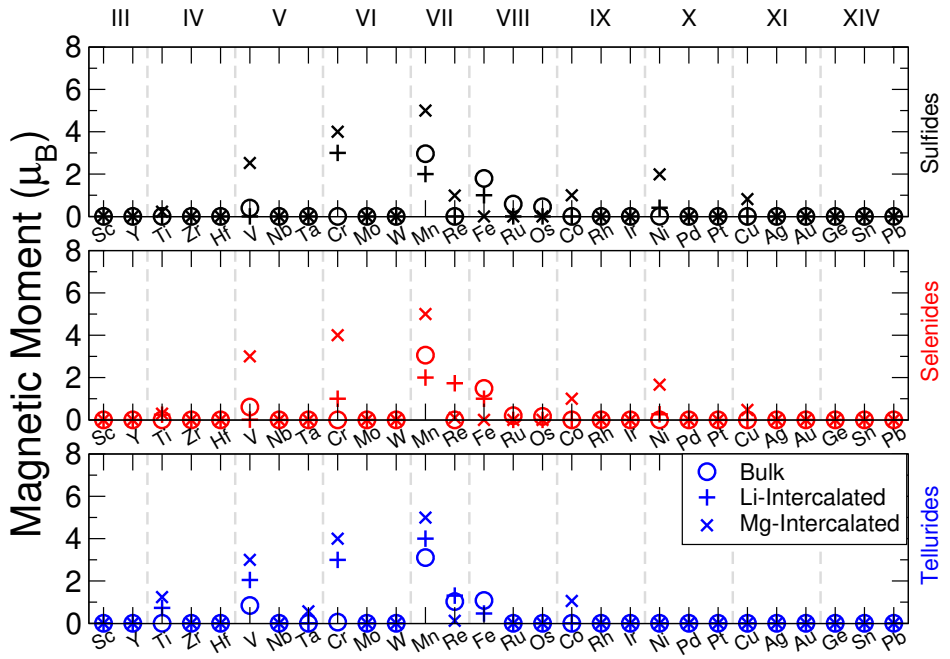

Figure S 35: Magnetic moment (per formula unit) of the different TMDCs explored. The sulfides (top), selenides (middle), and telluride (bottom) materials are included, with the results for lithium-intercalated structures presented with pluses, and magnesium-intercalated presented with crosses.

M. Spin

We present in Figure S35 the magnetic moments (per formula unit) for each of the TMDCs in their pristine and their $a = 1$ intercalated structures. We find that magnetic moments are only presented by TMDCs composed of central block transition metals (Groups V to X). Of these, the largest moments are shown by the top row transitions metals V, Cr, and Mn when their TMDCs are intercalated with magnesium, and when their tellurides are intercalated with lithium.

---

* cjp225@exeter.ac.uk

† S.P.Hepplestone@exeter.ac.uk

[1] P. E. Blöchl, Physical Review B **50**, 17953 (1994).

[2] H. J. Monkhorst and J. D. Pack, Physical Review B **13**, 5188 (1976).

[3] J. P. Perdew, K. Burke, and M. Ernzerhof, Physical Review Letters **77**, 3865 (1996).

[4] S. Grimme, J. Antony, S. Ehrlich, and H. Krieg, The Journal of Chemical Physics **132**, 154104 (2010).

[5] N. T. Taylor, C. J. Price, A. Petkov, M. I. Romanis Carr, J. C. Hale, and S. P. Hepplestone, Journal of Physical Chemistry Letters **11**, 4124 (2020).

[6] S. H. Wei and A. Zunger, Applied Physics Letters **72**, 2011 (1998).

[7] F. H. Davies, C. J. Price, N. T. Taylor, S. G. Davies, and S. P. Hepplestone, Physical Review B **103**, 1 (2021).

[8] M. K. Aydinol, A. F. Kohan, G. Ceder, K. Cho, and J. Joannopoulos, Physical Review B **56**, 1354 (1997).

[9] M. Mayo, K. J. Griffith, C. J. Pickard, and A. J. Morris, Chemistry of Materials **28**, 2011 (2016), arXiv:1510.03248.

[10] A. N. Enyashin and G. Seifert, Computational and Theoretical Chemistry **999**, 13 (2012).

[11] S. Fan, X. Zou, H. Du, L. Gan, C. Xu, W. Lv, Y. B. He, Q. H. Yang, F. Kang, and J. Li, Journal of Physical Chemistry C **121**, 13599 (2017).

[12] Z. Liu, H. Deng, and P. P. Mukherjee, ACS Applied Materials and Interfaces **7**, 4000 (2015).

[13] P. Gao, L. Wang, Y. Y. Zhang, Y. Huang, L. Liao, P. Sutter, K. Liu, D. Yu, and E. G. Wang, Nano Letters **16**, 5582 (2016).

[14] D. S. Tchitchekova, A. Ponrouch, R. Verrelli, T. Broux, C. Frontera, A. Sorrentino, F. Bardé, N. Biskup, M. E. Arroyo-de Dompablo, and M. R. Palacín, Chemistry of Materials **30**, 847 (2018).

[15] K. C. Woo, W. A. Kamitakahara, D. P. DiVincenzo, D. S. Robinson, H. Mertwoy, J. W. Milliken, and J. E. Fischer, Physical Review Letters **50**, 182 (1983).

[16] F. Zhou, M. Cococcioni, C. A. Marianetti, D. Morgan, and G. Ceder, Physical Review B - Condensed Matter and Materials Physics **70**, 1 (2004), arXiv:0406382 [cond-mat].

[17] V. L. Chevrier, S. P. Ong, R. Armiento, M. K. Chan, and G. Ceder, Physical Review B - Condensed Matter and Materials Physics **82**, 1 (2010).

[18] J. Heyd, G. E. Scuseria, and M. Ernzerhof, Journal of Chemical Physics **118**, 8207 (2003).

[19] J. Heyd, G. E. Scuseria, and M. Ernzerhof, "Erratum: Hybrid functionals based on a screened Coulomb potential (Journal of Chemical Physics (2003) 118 (8207))," (2006).

[20] J. Paier, M. Marsman, K. Hummer, G. Kresse, I. C. Gerber, and J. G. Angyán, Journal of Chemical Physics **124**, 154709 (2006).